An Inflated Ensemble Filter for Ocean Data Assimilation with a Biased Coupled GCM

S. ZHANG AND A. ROSATI

NOAA/Geophysical Fluid Dynamics Laboratory, Princeton University, Princeton, New Jersey

(Manuscript received 24 December 2009, in final form 19 March 2010)

ABSTRACT

A ''biased twin'' experiment using two coupled general circulation models (CGCMs) that are biased with respect to each other is used to study the impact of deep ocean bias on ensemble ocean data assimilation. The ''observations'' drawn from one CGCM based on the Argo network are assimilated into the other. Traditional ensemble filtering can successfully recover the upper-ocean temperature and salinity of the target model but it usually fails to converge in the deep ocean where the model bias is large compared to the ocean's intrinsic variability. The inconsistency between the well-constrained upper ocean and poorly constrained deep ocean generates spurious assimilation currents. An adaptively inflated ensemble filter is designed to enhance the consistency of upper- and deep-ocean adjustments, based on ''climatological'' standard deviations being adaptively updated by observations. The new algorithm reduces deep-ocean errors greatly, in particular, reducing current errors up to 70% and vertical motion errors up to 50%. Specifically, the tropical circulation is greatly improved with a better representation of the undercurrent, upwelling, and Western Boundary Current systems. The structure of the subtropical gyre is also substantially improved. Consequently, the new algorithm leads to better estimates of important global hydrographic features such as global overturning and pycnocline depth. Based on these improved estimates, decadal trends of basin-scale heat content and salinity as well as the seasonal–interannual variability of the tropical ocean are constructed coherently. Interestingly, the Indian Ocean (especially the north Indian Ocean), which is associated with stronger atmospheric feedbacks, is the most sensitive basin to the covariance formulation used in the assimilation. Also, while reconstruction of the local thermohaline structure plays a leading-order role in estimating the decadal trend of the Atlantic meridional overturning circulation (AMOC), more accurate estimates of the AMOC variability require coupled assimilation to produce coherently improved external forcings as well as internal heat and salt transport.

1. Introduction

Because of the lack of complete observations and the existence of uncertainties in climate modeling, data assimilation is needed to improve climate state estimates. The model uncertainties arise partly from inadequate measurements of natural and/or anthropogenic forcings, incomplete understanding of their radiative effects, as well as issues in the numerical implementation of physical and dynamical processes. Because of these uncertainties, models drift away from the real world, which leads to what is called model bias. Generally, observations provide only some samples of certain climate variables and are often sparse and noisy in time and space. To obtain a more realistic estimate for climate evolution, data assimilation uses model dynamics to extract observational information and reconstructs the historical and present states of climate. The reconstructed time series is fundamental to improving our understanding of observed climate changes and variations. Practically, the estimated states are used as initial conditions in numerical climate prediction and thus largely determine the accuracy of the predictions.

Combining the needs of state estimation and forecast initialization, the National Oceanic and Atmospheric Administration/Geophysical Fluid Dynamical Laboratory (NOAA/GFDL) uses its second generation fully-coupled model (CM2; Delworth et al. 2006) to implement climate data assimilation. A proof-of-concept study within a perfect model framework has been reported (Zhang et al. 2007). Based on *estimation theory* (Jazwinski, 1970), the GFDL coupled data assimilation (CDA) system directly solves for a temporally evolving joint probability distribution function (PDF) of climate states by combining the observational PDF and a prior PDF derived from the dynamically coupled model. The ensemble filter first

Corresponding author address: Shaoqing Zhang, NOAA/GFDL, Princeton University, P.O. Box 308, Princeton, NJ 08542.
E-mail: shaoqing.zhang@noaa.gov

DOI: 10.1175/2010MWR3326.1

simulates the prior PDF by a Monte Carlo approach (i.e., launching a set of model integrations). Then the state of each ensemble member is adjusted by observations through a multivariate linear regression based on the first (expectation) and second (covariance) moments of the prior joint PDF, keeping all higher-order moments unchanged. This adjustment scheme maintains the physical balance between state variables (Kalnay 2003) and sustains the feature of the nonlinearity of long-term climate evolution (Anderson 2001, 2003; Anderson et al. 2009). Instantaneously exchanged information among all coupled components is expected to minimize coupling initial shocks when the coupled model is initialized for numerical climate prediction using the CDA-generated ensemble initial conditions (Zhang et al. 2007, 2008, 2009).

Two outstanding issues in climate state estimation combining model and data need to be addressed: the representation of observing systems (e.g., Zhang et al. 2009) and the impact of model bias (e.g., Dee and Silva 1998; Dee 2005). Generally, a fundamental approach to deal with the model bias issue in ocean data assimilation (ODA) is the statistical bias correction (e.g., Cherupin et al. 2005; Kepenne et al. 2005; Balmaseda et al. 2007). Alternative approaches to relax the model bias issue of data assimilation include 1) increasing uncertainties of low modes in initial conditions by analyzing the initial error subspace (e.g., Lermusiaux 2002), and 2) filtering inflation (e.g., Anderson 2007; Lermusiaux 2006, 2007; Uzunoglu et al. 2007; Counillon et al. 2009), in terms of broadening the representation of unbiased forecast error covariances. However, understanding the impact of deep-ocean bias on ocean state estimation is particularly challenging. On the one hand, because of the lack of deep-ocean observations (e.g., the modern twenty-first-century Argo system samples the ocean temperature and salinity only down to 2000 m), it is difficult to explicitly define deep-ocean bias (Dee 2005). On the other hand, clearly identifying data-sampled signals and bias-induced artifacts from the assimilation-generated variability is even more difficult because of the imperfection of both observations and model.

To address the impact of deep-ocean bias on ODA with a coupled general circulation model (CGCM), this study first introduces a ''biased twin'' experiment using two CGCMs that are biased with respect to each other, which will be described in section 2. In this biased-twin experiment, the ''observations'' that are drawn from the simulation of one CGCM, according to the locations and times of Argo observations, are assimilated into the other CGCM. In such a twin experiment, the model bias in the deep ocean is explicitly defined and the bias-induced artifacts in the assimilation-generated variability can be distinguished quantitatively by comparing the assimilation product with the ''truth'' from which observations are drawn. Section 3 addresses a general problem induced by deep-ocean bias in traditional ensemble ODA. Section 4 designs an adaptively inflated ensemble filtering scheme to increase deep-ocean constraints coherently so as to relax the problem. In section 5, based on the results of 25-yr parallel assimilations from both the traditional and new schemes, the impact of the new scheme on the estimation of oceanic climate features and variability are thoroughly evaluated. Summary and discussions are given in section 6.

2. Experimental design

a. Two biased CGCMs at GFDL

Combining two atmosphere models, atmospheric and land model versions 2.0 (AM2.0/LM2.0) and 2.1 (AM2.1/LM2.1), with the fourth version of Modular Ocean Model (MOM4) and Sea Ice Simulator (SIS), GFDL has developed two fully-coupled general circulation models (CGCMs): CM2.0 and CM2.1 (Delworth et al. 2006). These two atmosphere models are based on different dynamical cores: B-grid finite difference (Wyman 1996; GFDL Global Atmospheric Model Development Team 2004) for AM2.0 and finite volume (Lin 2004) for AM2.1. Both have the same vertical (24 levels) and horizontal (2.5° longitude by 2° latitude) resolution, as well as an identical physical package and land model. These two coupled models have their own tuned parameters in both the atmosphere and ocean.

The MOM4 is configured with 50 vertical levels (22 levels of 10-m thickness in the top 220 m), 1° × 1° horizontal B-grid resolution telescoping to 1/3° meridional spacing near the equator. The model has an explicit free surface with freshwater fluxes exchanged between the atmosphere and ocean. Parameterized physical processes include *K*-profile parameterization (KPP) vertical mixing, neutral physics, a spatially dependent anisotropic viscosity, and a shortwave radiative penetration depth that depends on a prescribed climatological ocean color. Insolation varies diurnally and the wind stress at the ocean surface is computed using the velocity of the wind relative to surface currents. An efficient time-stepping scheme (Griffies 2005) is employed. The SIS in the coupled model is a dynamical ice model with three vertical layers (one for snow and two for ice) and five ice-thickness categories. The elastic–viscous–plastic technique (Hunke and Dukowicz 1997) is used to calculate ice internal stresses, and the thermodynamics is a modified Semtner three-layer scheme (Winton 2000).

Details of the simulated oceans in CM2.0 and CM2.1 can be found in Gnanadesikan et al. (2006). Here we

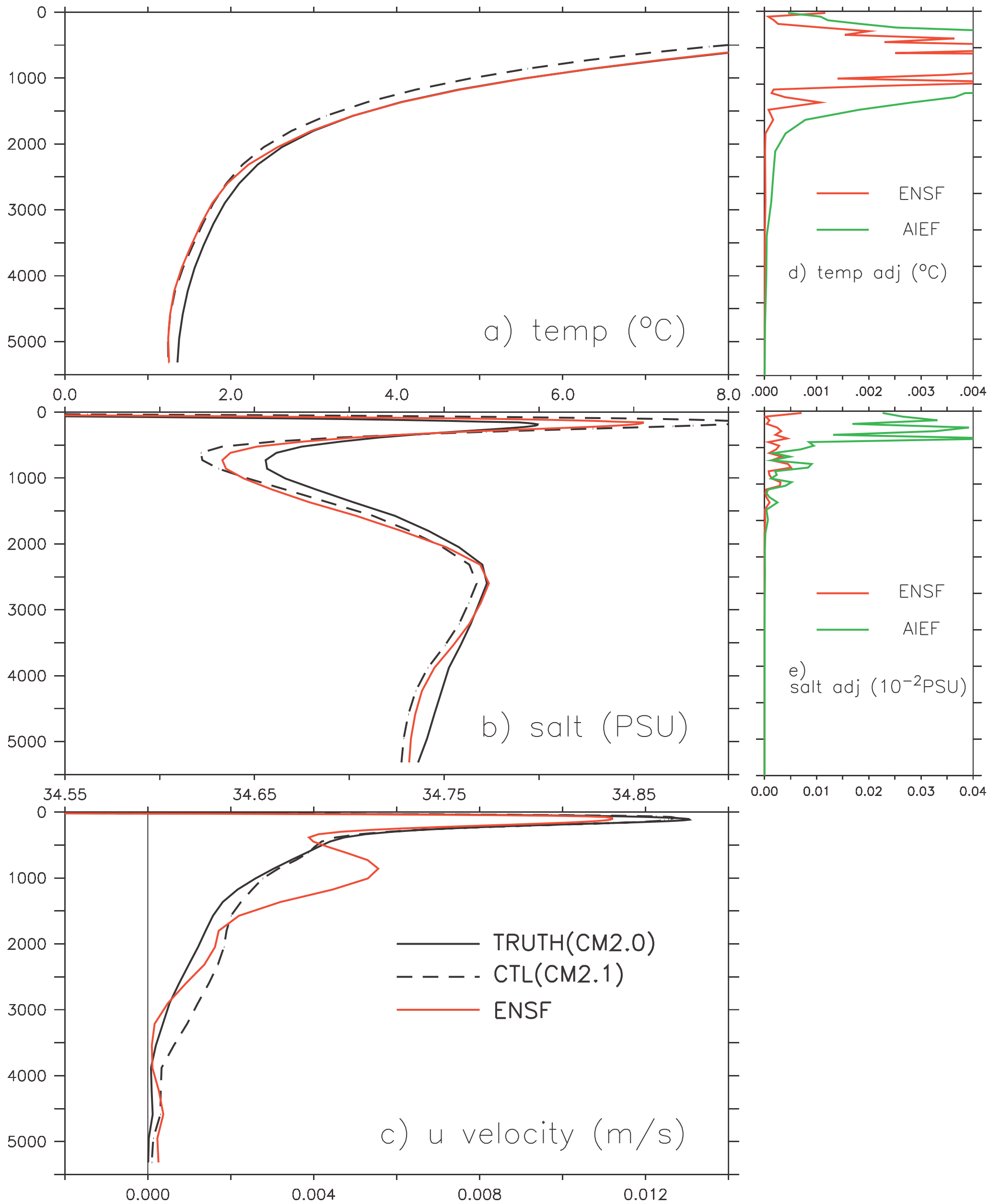

FIG. 1. Global mean (a) temperature (T), (b) salinity (S), and (c) u-velocity profiles averaged over the last 20 yr in the 140-yr model simulation produced by CM2.0 (solid black, also denoted by TRUTH) and CM2.1 (dashed black, also denoted by CTL). Both models use historical (temporally varying) greenhouse gas and natural aerosol radiative forcings and start from the same coupled initial conditions at 0000 UTC 1 Jan 1861 reset from a previous study (Stouffer et al. 2004). The red line is produced by the traditional ensemble filter (ENSF) assimilation. The annual mean rms of (d) temperature and (e) salinity adjustments over the tropical (20°S–20°N) Pacific produced by the 12-member ENSF (red) and AIEF (green) in a 5-yr (1976–80) test period.

only comment on a fundamental characteristic—their bias with respect to each other. Figures 1a,b present the time-averaged global mean temperature and salinity profiles over the last 25 yr from the 140-yr integrations of CM2.0 (solid black) and CM2.1 (dashed black) in the Intergovernmental Panel on Climate Change (IPCC) Fourth Assessment Report (AR4) historical simulations (Randall et al. 2007). Both models use historical greenhouse gas and natural aerosol (GHGNA) radiative forcings (the date of GHGNA records is referred as the model calendar) and start from the same coupled initial conditions. The initial conditions are taken from the previous study of Stouffer et al. 2004 and the date is set as 1 January 1861. Figures 1a,b show that over 1–6 km the global mean bias of CM2.1 is about 0.2°C colder and 0.01 PSU fresher than in CM2.0. This relative ocean bias mainly comes from the entirely different atmospheric model (dynamical core and cloud parameters) in each coupled system, but it is also associated with different ocean model parameters. Since the deep-ocean biases have a geographic dependence (e.g., 0.35°C and 0.04 PSU for the South Pacific and −0.36°C and −0.15 PSU for the North Atlantic), we show in this study that they significantly affect the quality of ocean assimilation even if the global bias at depth is small compared to the real model bias relative to observations (Delworth et al. 2006).

b. Coupled ensemble filter

The probabilistic nature of state evolution of a coupled model system is the basis of implementing ensemble coupled data assimilation. The theory of *filtering* (Jazwinski 1970) views the temporal evolution of coupled model states as a continuous stochastic dynamical process described by a vectorized stochastic differential equation, $d\mathbf{x}_t/dt = \mathbf{f}(\mathbf{x}_t, t) + \mathbf{G}(\mathbf{x}_t, t)\mathbf{w}_t$. Here, $\mathbf{x}_t$ is an n-dimensional vector representing the coupled model state at time t (n is the size of the model state), $\mathbf{f}$ is an n-dimensional vector function, $\mathbf{w}_t$ is a white Gaussian process (uncorrelated in time) of dimension r with mean 0 and covariance matrix $\mathbf{S}(t)$, while $\mathbf{G}$ is an $n \times r$ matrix that defines the relation of the white Gaussian process and $\mathbf{x}_t$. The first and second terms of the right-hand side in the equation represent the contributions of deterministic modeling and uncertainties of modeling respectively. Based on a background joint PDF of climate states provided by a dynamical model, Bayes's rule is used to produce an analyzed PDF by combining the model-derived prior PDF and observational PDF. Ensemble-based filters use a Monte Carlo approach to simulate the prior PDF through finite-ensemble model integrations.

As described in Zhang et al. (2007), in a two-step local least squares filtering implementation (Anderson 2003), at the first step, the observational increment for the ith ensemble member produced by the kth observation, $\Delta y_{i,k}^o$, is computed [manipulated from Eqs. (2)–(5) in Zhang et al. (2007)] as

$$\Delta y_{i,k}^o = \frac{\overline{y}_k}{1+\kappa^2(y_k, y_k^o)} + \frac{y_k^o}{1+\kappa^{-2}(y_k, y_k^o)} + \frac{y_{i,k}-\overline{y}_k}{\sqrt{1+\kappa^2(y_k, y_k^o)}} - y_{i,k}, \quad (1)$$

where the first two terms on the right-hand side represent the shift of ensemble mean and the third term is the adjustment of ensemble spread, given a Gaussian observation $N(y_k^o, \sigma_k^o)$. Here y_k is the model estimate for observation y_k^o and an overbar represents the ensemble mean. Here $\kappa(y_k, y_k^o)$ is the ratio of standard deviations of the model ensemble and the observational error at location k, that is, σ_k/σ_k^o. Note that under a perfect model assumption, the observational increment expressed by Eq. (1) is only a function of forecast error variances, and it does not account for the systematic model uncertainty (bias).

At the second step, any oceanic state variable at gridpoint j for the ith ensemble member $x_{i,j}$ is adjusted [expanded from Eq. (6) in Zhang et al. (2007) to include the covariance localization in Appendix A] as

$$\Delta x_{i,j} = \Omega_{j,k}\frac{\mathrm{Cov}(x_j, y_k)}{\sigma_{y_k}^2}\Delta y_{i,k}^o = \Omega_{j,k} r(x_j, y_k)\Delta y_{i,k}^o = \Omega_{j,k}\rho(x_j, y_k)\frac{\sigma_{x_j}}{\sigma_{y_k}}\Delta y_{i,k}^o = \Omega_{j,k}\rho(x_j, y_k)\kappa(x_j, y_k)\Delta y_{i,k}^o. \quad (2)$$

Here $\rho(x_j, y_k)$ and $r(x_j, y_k)$ represent the correlation coefficient and linear regression coefficient between x_j and y_k, respectively. The $\kappa(x_j, y_k)$ is the ratio of the ensemble-estimated standard deviations for x_j and y_k. The Ω is the covariance localization function [Appendix A, see also Zhang et al. (2005)], which is only determined by the distance between locations j, k. Note all error statistics used here, $\mathrm{Cov}(x_j, y_k)$, $\rho(x_j, y_k)$, σ_{y_k}, σ_{x_j}, and $r(x_j, y_k)$, are evaluated by the model ensemble and thus are a function of space and time. This means that the background covariances used in the filtering are anisotropic and temporally varying. For simplicity, the common time subscript t in all terms of Eq. (2) has been dropped.

The ensemble filter outlined above has a few advantages for oceanic climate studies. First, the filtering conducts a multivariate analysis based on the prior joint PDF and maintains the physical balance required by model equations when data are blended into the model dynamics. Second, the temporally evolving and spatially anisotropic error covariances used at each analysis step allow the assimilation to capture the features of local waves and vertical variations of oceanic circulations. Third, the filtering uses data to adjust the probability distribution of climate states only up to the second-order moments from the prior PDF but keeps all higher-order moments unchanged. This sustains the nonlinearity in a long-term evolution of oceanic circulations. For example, an ensemble coupled data assimilation system may maintain the bimodal feature of the Atlantic meridional overturning circulation (AMOC), which reflects the regime transition between active and inactive overturnings in the longtime evolution of the AMOC. Finally the instantaneously exchanged fluxes in a coupled system transfer observational information into all coupled components. It is expected that such a coupled ensemble data assimilation system can minimize coupling shocks in ensemble initialization.

The *filtering* theory described above assumes that both the dynamical model and ensemble sampling of PDF are perfect. In practice, the dynamical model is however biased and the ensemble integration time and ensemble size are not infinite. A finite ensemble always has a different representation for error statistics of oceanic circulations at different depth. Next, starting from a twin experiment using two biased CGCMs, we present the impact of deep-ocean bias on ensemble ODA.

c. Biased-twin ODA experiment with CGCMs

To examine the performance of an ensemble filtering ODA when the assimilation model is biased, we use one CGCM to produce the ''true'' climate variation and the corresponding observations, and the other to assimilate these observations in order to recover the truth. This assimilation will be referred to as the biased-twin experiment as model bias is unambiguously defined and the bias-generated variability in assimilation can be estimated quantitatively. As in Zhang et al. (2009), the GFDL's IPCC historical simulation produced by CM2.0 is set as the target (hereafter TRUTH) of assimilations. Another set of IPCC model integrations starting from the same initial conditions and with the same GHGNA radiative forcings, but produced by CM2.1, is used as a free model control (hereafter CTL). The CTL simulation does not include any data constraint and will serve as a reference to evaluate the assimilations, and is also used to form ensemble initial conditions from which the assimilation starts. The ensemble initial conditions are a set of atmospheric (including land) states taken at 1-yr intervals combined with a common oceanic (including sea ice) state. For example, the initial conditions of the 24-member ensemble are formed by combining the atmospheric and land states at 0000 UTC 1 January of 1964–87 with the oceanic and sea ice states at 0000 UTC 1 January 1976. The quality of the assimilation using 6-, 12-, and 24-member ensembles during a 5-yr test period was compared. Probably related to the particular model and data resolution as well as the strong localization in the filtering, no significant improvement was found from a 12-member ensemble to a 24-member ensemble. Based on this result, a 12-member ensemble is used for all assimilation experiments. Note that the calendar date in this study refers to the model calendar that is defined by the historical GHGNA records.

The observing system used in this study is the twenty-first-century Argo network. First the IPCC integration is rerun using the updated version of CM2.0 starting from 1 January 1976 up to 31 December 2000 to prepare daily data of oceanic temperature and salinity. These model data are projected onto the 2005 Argo network through a trilinear interpolation to sample the truth based on the Argo's locations and depth (see Zhang et al. 2007, 2009) so that, as for most of the real Argo array, the data (observations) used in this study are restricted to 2000 m. Once oceanic observations (again, produced by CM2.0) and ensemble initial conditions (from CM2.1) are ready, using the CM2.1 model with the ensemble filter described in section 2b, the biased-twin ODA experiment is conducted. Except for the following two aspects that are new for this biased case, the traditional ensemble filtering ODA algorithm (hereafter briefly as ENSF) used here is the same as before in Zhang et al. (2007, 2009):

1) To reduce the assimilation adjustment initial shock, the daily adjustment is evenly distributed onto each time integration step instead of only being added daily. In previous perfect model studies, the adjustment shocks did not cause any serious problem, but in this biased case, the amplitude is bigger and shocks can significantly degrade the quality of assimilation without doing so.
2) The adjustment of currents (U, V) based on cross covariances between T, S and U, V is converted into an acceleration amount and added into the time tendency of velocity update equations. In this way, the barotropic and baroclinic modes are updated consistently as the model integrates forward, which minimizes possible computational modes induced by adjusting the velocity itself.

3. Impact of deep-ocean bias on ensemble ODA

a. Too small ensemble spread versus model bias in deep ocean

The coupled system with the ensemble ODA is run for 25 yr (January 1976–December 2000). Two particular phenomena stand out when comparing the ENSF assimilation errors to the CTL errors: 1) while the assimilation dramatically reduces the errors of temperature and salinity (Figs. 2a,b), the errors in the simulated currents (Figs. 2c,d) and vertical motions (Fig. 2e) are increased in the ocean interior; 2) the rate of error reduction of temperature and salinity from CTL to ENSF has a strong depth dependency and the largest error reduction is found between 500 m and 2 km. Consistently, while the temperature and salinity errors in

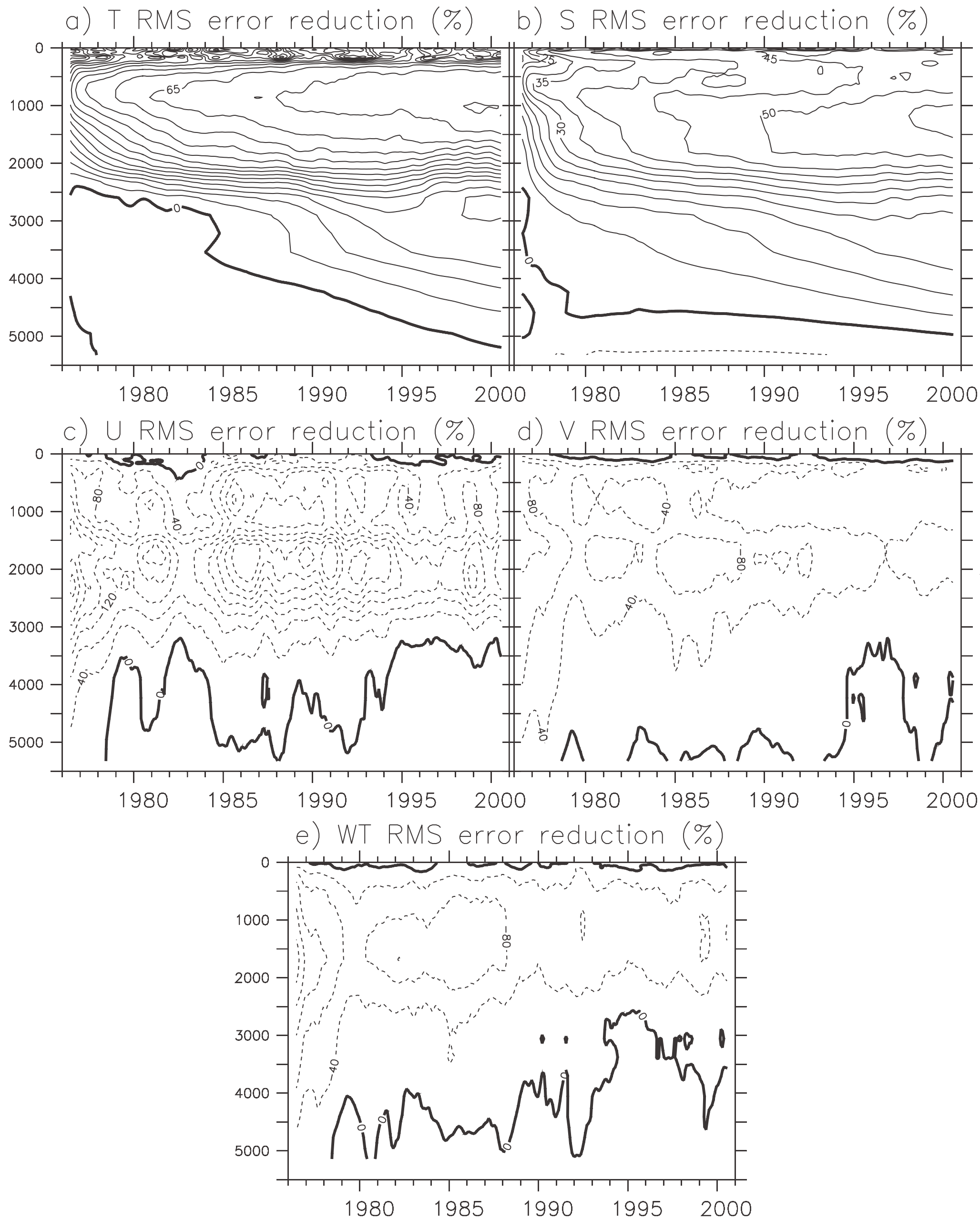

FIG. 2. Time series of the global rms error reduction (%) from the model control (CTL), produced by the ENSF assimilation in the GFDL's coupled system for oceanic (a) temperature, (b) salinity, (c) u component of currents, (d) v component of currents, and (e) vertical motions. The "truth" is the IPCC AR4 historical simulation produced by CM2.0 (see section 2a) and "observations" are produced by using the 2005 Argo network to sample the truth. Then these observations are assimilated into CM2.1 (see section 2a) for recovering the truth. The contour interval is 5% in (a),(b) and 40% in (c)–(e). A 10-month running mean is applied for graphing.

ENSF increase with depth, the temperature and salinity profiles of ENSF are closer to the profiles of CTL (Figs. 1a,b). Currents and vertical motions diverge from TRUTH primarily when the rate of error reduction of temperature and salinity of ENSF rapidly decreases with depth (cf. Figs. 2c–e and 2a,b).

To understand the behavior of the ENSF assimilation, we first analyze the ability of a finite ensemble to represent the upper- and deep-ocean variability. Figure 3 presents the time mean ensemble spread (first 6 members) of atmospheric and oceanic states over the last 10 yr of a 25-yr free ensemble integration of CM2.1. The

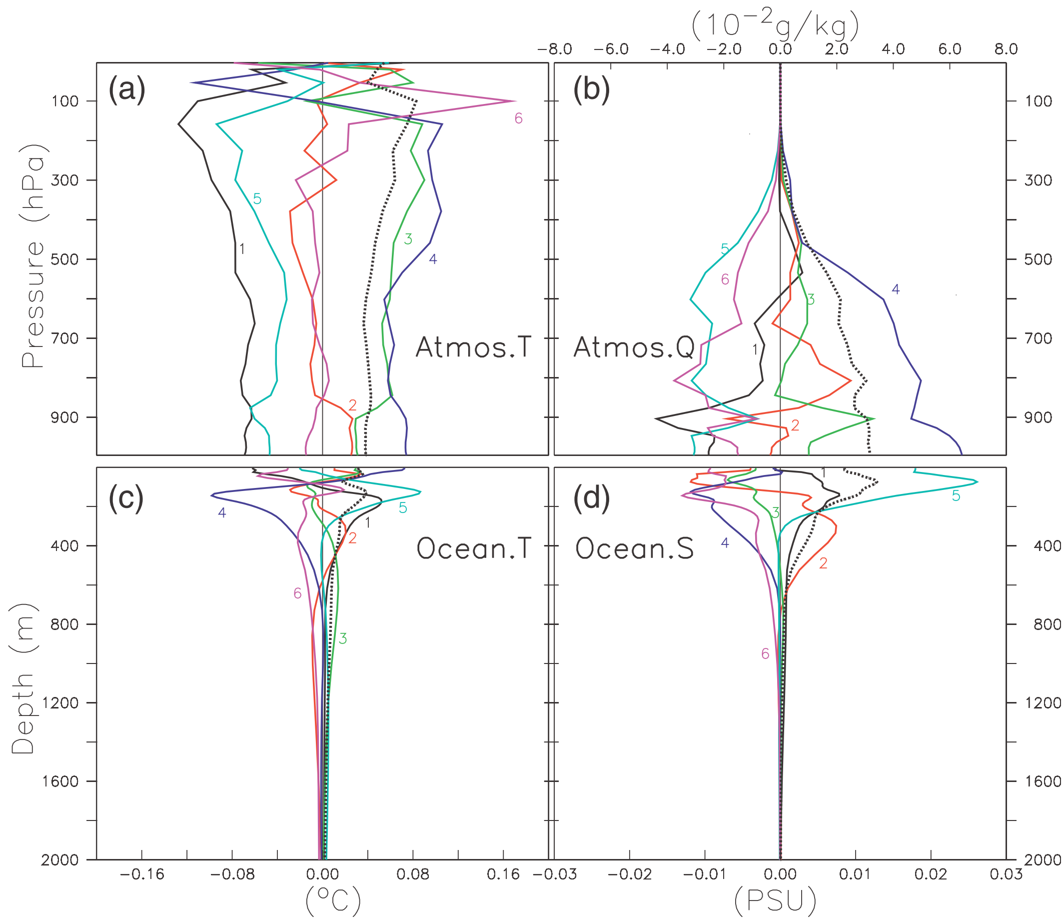

FIG. 3. The ensemble spread of the (a),(b) atmosphere and (c),(d) ocean in CM2.1. Each solid line represents the departure of individual ensemble member (marked by a member index) from the ensemble mean (only the first 6 members are shown) of the global mean (a) atmospheric and (c) oceanic temperature, (b) atmospheric specific humidity, and (d) oceanic salinity averaged over the last 10 yr during a 25-yr ensemble integration. The coupled model ensemble is initialized from 12 atmospheric states (including land) taken at 1-yr intervals combining with a common oceanic state (including sea ice). The dotted black lines are the standard deviation of the corresponding ensemble spread computed by the 12-member ensemble.

ensemble is initialized from atmospheric (including land) states taken at 1-yr intervals combined with a common oceanic (including sea ice) state (see section 2c). Each solid line (different color) represents the departure of an individual member's atmospheric–oceanic (Figs. 3a–d) temperature profile (Figs. 3a,c) or atmospheric-specific-humidity–oceanic-salinity profile (Figs. 3b,d) from the ensemble mean. The dotted black line in each panel shows the vertical variation of the ensemble standard deviation. Because of the strong internal variability in the atmosphere, perturbations in both initial conditions and model-generated SSTs (as a consequence of ocean–atmosphere interaction) maintain the ensemble spread of the atmospheric states, which is nearly uniform in the vertical.

Unlike the ensemble spread of the atmosphere, which results from its strong internal variability, the ensemble spread of the ocean in this model reflects the sensitivity of ocean circulations to the surface forcings provided by the atmosphere. Because of effects of mixing and convection, the atmospheric disturbances can easily penetrate the upper ocean and alter the thermocline distribution, where the largest oceanic spread is observed. In fact, the ensemble spread of oceanic temperatures near the surface has the same order of magnitude as that of atmospheric temperatures in the lower troposphere. For each ensemble member, while the temperature shows a nearly continuous variation at the air–sea interface, the specific humidity and oceanic salinity shows a discontinuity at the interface. This different correlation pattern reflects the nature of atmosphere–ocean coupling [i.e., the atmosphere responds to SST but not to sea surface salinity (SSS), while the SSS variability is strongly influenced from precipitation, especially in the tropics]. Figure 3 also shows that the ensemble spread decreases dramatically with depth below the thermocline, and compared to model bias, it rapidly becomes trivial below 1000 m. When the model ensemble spread is very small, as described in Eq. (1), the observational increment, $\Delta y_{i,k}^o$, becomes trivial because $\kappa(y_k, y_k^o) \approx 0$ as $\sigma_k \ll \sigma_k^o$. Then the model is overconfident so that it rejects data (i.e., $\Delta x_{i,j} \approx 0$). Thus, the assimilation diverges from TRUTH.

b. Spurious currents induced from the incoherent vertical structure of ODA adjustments

When the upper ocean is converging to data while the deep ocean is rejecting data because of a too small ensemble spread in deep ocean as described in the last section, ENSF constructs an incoherent vertical structure between the well-constrained upper ocean and the poorly constrained deep ocean in a biased assimilation model. Note that pressure (water mass) at a certain depth is the vertical integral of the density, which is a function of temperature and salinity. The pressure gradient is thus determined by the horizontal distribution of water masses at depth. The incoherent vertical structure of data adjustments on temperature and salinity produces an incorrect horizontal distribution of water mass, which leads to incorrect pressure gradient and spurious velocities as shown in Fig. 1c. The maximum spurious velocity appears between 500 and 2000 m corresponding to the layer where the convergence rate of temperature and salinity dramatically decreases with depth (cf. Figs. 2c,d and 2a,b). The velocities near the surface and bottom appear slightly improved. The improvement of currents near the surface can be explained by the ODA-improved mixing layer while the improvement at the bottom may be associated with better surface forcings (as a consequence of the atmospheric responses to the ODA-generated SSTs) through the joint effect of baroclinicity and bottom relief (JEBAR; see e.g., Myers et al. 1996).

When geostrophy holds, pressure gradient is a dominant factor to determine ocean currents while vertical motions are induced by the convergence and/or divergence of currents. Recovering currents requires higher-order accuracy than recovering temperature and salinity and it is even more difficult to recover vertical motions. Figures 1c and 2c–e show that while the temperature and salinity are convergent to the data over the upper oceans, the ENSF-generated pressure gradient is not.

4. AIEF—Adaptively inflated ensemble filter

a. Algorithm design

Covariance inflation is a common approach (Anderson and Anderson 1999; Anderson 2007; Zhang and Anderson 2003) to improve the performance of ensemble filters when the ensemble spread is small and the filter diverges. However, the implementation of the inflation technique requires a very cautious examination of the geofluid system to which it is applied.

First, given the character of variability of oceanic circulations at different depth, as shown in Fig. 3, the method applied to simple models in which a globally uniform coefficient is used to inflate the prior ensemble (Anderson and Anderson 1999; Anderson 2007; Zhang and Anderson 2003), may not be applicable for the ODA with a coarse-resolution ocean model in this CGCM. Moreover, for the noneddy-resolving ocean model that has small internal variability, directly inflating the perturbed surface forcings is inadequate to represent the model forecast uncertainty, especially with small ensemble sizes. Here we define a specific application of covariance inflation according to the features of GFDL's coupled ensemble system (Zhang et al. 2007) using an adaptive idea (Leslie et al. 2008), instead of including a stochastic internal forcing to model the oceanic uncertainties (Lermusiaux 2006).

Starting from a model simulated ''climatological'' standard deviation, the new algorithm adaptively inflates the prior ensemble according to the results of data assimilation. First, a first guess of climatological standard deviation is computed using a long time series of anomalies in a simulation of the assimilation model. The climatological standard deviation at depth reflects the variability resulting from the longtime response of the ocean model to sea surface forcings. After a period of assimilation spinup (usually 5 yr), the climatological standard deviation (called σ_0), which is used to inflate the prior ensemble in the filtering, is updated by the assimilation product every year. Then, the new filtering equation can be written as

$$\Delta x_{i,j} = \begin{cases} \Omega_{j,k}\rho_t(x_j, y_k) \quad \kappa_t(x_j, y_k)\Delta y_{i,k,t}^o, & Z \le Z_0 \\ \Omega_{j,k}\rho_t(x_j, y_k) \quad \left[\dfrac{(1-\alpha)\kappa_t(x_j, y_k)}{(1-\alpha)\kappa_t(x_j, y_k) + \alpha\kappa_0(x_j, y_k)}\kappa_t(x_j, y_k)\Delta y_{i,k,t}^o \right. & \\ \qquad \left. + \dfrac{\alpha\kappa_0(x_j, y_k)}{(1-\alpha)\kappa_t(x_j, y_k) + \alpha\kappa_0(x_j, y_k)}\kappa_0(x_j, y_k)\Delta y_{i,k,0}^o\right], & Z > Z_0 \end{cases} \tag{3}$$

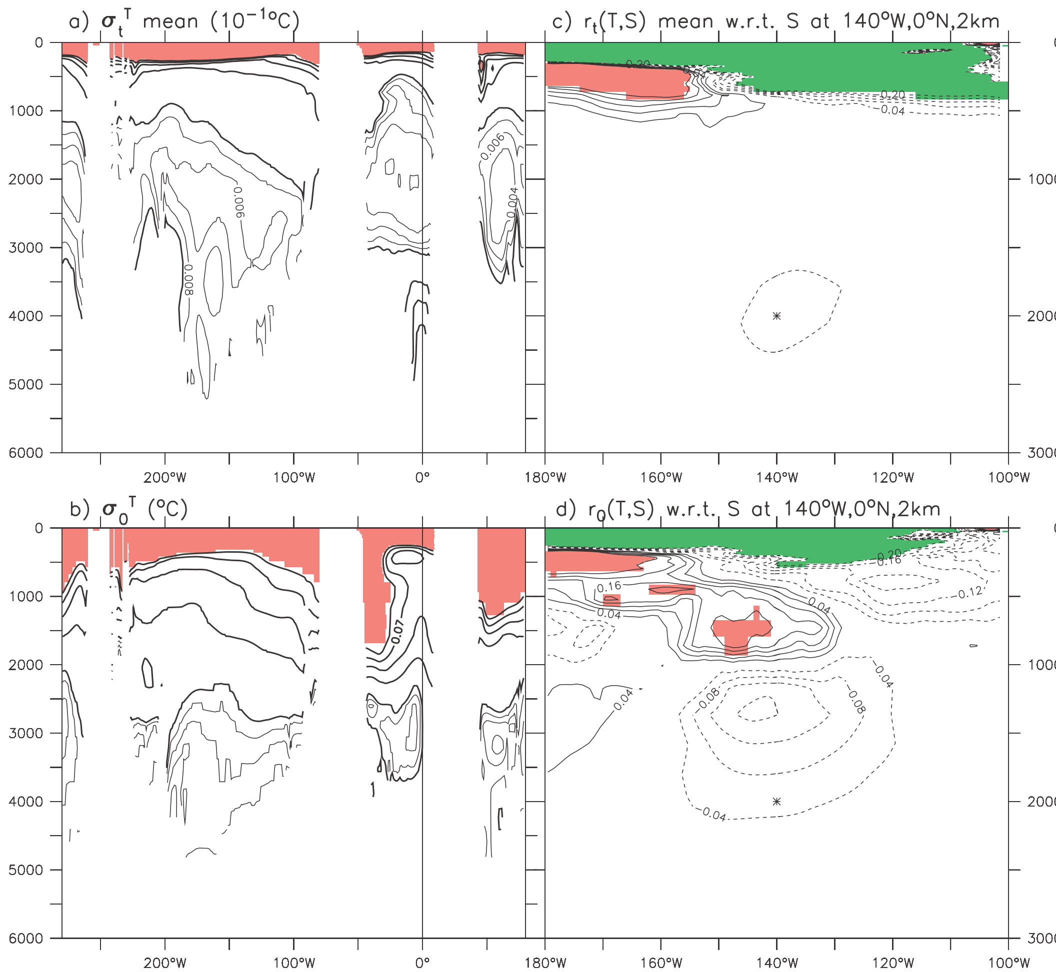

FIG. 4. Standard deviations of oceanic temperature evaluated by (a) a 12-member ensemble (the time mean over 20 yr) (called σ_t mean) and (b) a time series of 25-yr monthly mean anomalies of a model simulation (called σ_0) in the x–z plane at the equator. The contour interval is 0.02 (0.002) (°C) above (below) 0.01 (°C), and σ_t is multiplied by 10 for graphing. Linear regression coefficients between temperature and salinity given a salinity observation at (140°W, 0, 2 km) computed using (c) $\kappa_t(T, S)$ and (d) $\kappa_0(T, S)$ [see Eq. (3)] in the x–z plane at the equator. The contour interval is 0.04 (PSU °C^{-1}) and the regions where the values are > (<) 0.2 (−0.2) (PSU °C^{-1}) are shaded as red (green).

and

$$\Omega_{j,k} = \begin{cases} \Omega(a^h, d^h_{j,k})\Omega(a^v, d^v_{j,k}), & D^o \neq D^o_{\text{bottom}} \quad \text{or} \quad D^o = D^o_{\text{bottom}} \quad \text{but} \quad Z \le D^o_{\text{bottom}} \\ \Omega(a^h, d^h_{j,k})\Omega(a^v_b, d^v_{j,k}), & D^o \neq D^o_{\text{bottom}} \quad \text{and} \quad Z > D^o_{\text{bottom}} \end{cases}. \tag{4}$$

Here $\kappa_0(x_j, y_k)$ is the ratio of the values of σ_0 for x_j and y_k and correspondingly $\kappa_t(x_j, y_k)$ is the ratio of the values of σ_t for x_j and y_k, where σ_t is the standard deviation evaluated by the model ensemble. Here $\Delta y^o_{i,k,0}$ is the observational increment computed by σ_0 [the prior background standard deviation, σ_k, in Eq. (1), is replaced by the corresponding $\sigma_{k,0}$]. Here a^h and a^v are the e-folding horizontal and vertical scales in the covariance localization function (see Table 2 for their typical values), and $d^h_{j,k}$ and $d^v_{j,k}$ are the horizontal and vertical distance between x_j and y_k. Here D^o and D^o_{bottom} represent, respectively, the current observation depth and the maximum depth of an observed profile, and Z is the vertical coordinate. The first tunable parameter, Z_0, is the threshold depth of using σ_0. The second tunable parameter, a^v_b, is the vertical scale of the impact of the adjustment produced at the bottom of an observed profile. It is an important parameter to address how to

TABLE 1. Experiments for tuning AIEF.

Expt name	Z_0	a_b^v	Inflation domain
$AIEF_0$	1 km	$a_b^{v,0}(\approx 1$ km)	Global
$AIEF_1$	1 km	$2a_b^{v,0}(\approx 2$ km)	Global
$AIEF_2$	500 m	$2a_b^{v,0}(\approx 2$ km)	Global
$AIEF_3$	500 m	$4a_b^{v,0}(\approx 4$ km)	Global
$AIEF_4$	0	$4a_b^{v,0}(\approx 4$ km)	20°S–20°N [20°N(S)–25°N(S) for transition] for 1985–2000 in long run, otherwise global

coherently extend the adjustments at the bottom of observed profiles to deeper ocean. Here α is used to set an on–off switch for the inflation.

In this study, Z_0 is set as a globally uniform value as a first version with the application of the weighting combination technique in Eq. (3), although it could be a function of geographic location. Obviously, if Z_0 is set to be greater than the bottom of the model ocean (5316 m in CM2 models), this algorithm is degraded to the traditional ensemble filter. Here, a^v is defined by the thickness of a grid box, allowing two model levels below and above the current observation depth to be impacted by the observation at most. The application of parameter a_b^v is a little complicated to deal with different observational profiles. The basic values of a_b^v in our ensemble ODA (e.g., Zhang et al. 2007, 2009) is set based on the depth of a profile in 4 situations, called $a_b^{v,0}$: case 1 $-a_b^{v,0} = a^v$ when D_{bottom}^o is less than 500 m; case 2 $-a_b^{v,0} = a^v$ plus 1 more model level when D_{bottom}^o is between 500 m and 1 km; case 3 $-a_b^{v,0} = a^v$ plus 2 more model levels when D_{bottom}^o is between 1 and 2 km; and case 4 $-a_b^{v,0} = a^v$ plus 3 more model levels when D_{bottom}^o is equal to or greater than 2 km. For example, the value of $a_b^{v,0}$ is about 1000 m as $D_{\text{bottom}}^o = 2$ km for most of the Argo profiles. Note, because of the underdetermination of deep-ocean variance by a finite ensemble in ENSF, the adjustment at the bottom of an Argo profile is so small that increasing the a_b^v value does not strengthen the adjustments below the bottom of profiles except for a refined ramp for the adjustment from the bottom of observed profiles. In the new algorithm since the magnitude of deep-ocean adjustments is enlarged by $\kappa_0(x_j, y_k)$, a_b^v becomes an important parameter for enhancing the consistency of assimilation adjustments, which will be tested in section 4b.

Figures 4a,b give an example of the time mean standard deviation evaluated by the ensemble $[\sigma_t]$ compared to the climatological standard deviation (σ_0) of ocean temperature anomalies. From Figs. 4a,b, it is observed that σ_0 is one order of magnitude greater than $[\sigma_t]$. This kind of inflation is performed according to what the climatological variability of deep-ocean circulations allows. In addition, in order to mostly sustain the temporally evolving nature of upper-ocean covariances and model physical balances, the new algorithm consists of a weighted combination of uninflated and inflated adjustments as shown in Eq. (3) with $\alpha = 0.5$. The σ_0 that is used in Eq. (3) for the filtering inflation is updated as the average of σ_0^p (the climatological standard deviation from the last update) and $[\sigma_t]$. In this way, the filtering inflation adaptively takes the effect of data-defined variability as the assimilation proceeds.

Figures 4c,d gives an example of the relative amplitude of the time mean of $r_{tt}(T, S)$ (Fig. 4c) computed from $\kappa_t(T, S)$ and $\rho_t(T, S)$ and $r_{t,0}(T, S)$ (Fig. 4d) computed from $\kappa_0(T, S)$ and $\rho_t(T, S)$. In the tropical oceans, the signals in the time mean of $r_{t,0}(T, S)$ appear very weak below 500 m, while the signals in the time mean of $r_{t,0}(T, S)$ are much stronger and extending down to 3 km. By compensation, the new algorithm may let the linear regression coefficients used in the filtering take into account the strength of $r_{t,0}(T, S)$ below 500 m. On the contrary, in the mid- and high latitudes (not shown), because of the existence of the strong variability of gyres, the time mean of $r_{tt}(T, S)$ shows stronger signals than the $r_{t,0}(T, S)$ in the regions of subtropical and subpolar gyres. Given this circumstance, it may be reasonable to keep the temporally varying information of $r_{tt}(T, S)$ in the filtering. This issue will also be examined in section 4b.

TABLE 2. Values of parameters in Eq. (3) used in section 5.

Name	Physical meaning	Value range	Typical value	Value in this study
α	On–off switch for inflation	[0, 1]	0.5	0.5 in 20°S, 20°N, 0.5–0 in 20°N(S), 25°N(S), elsewhere 0
Z_0	Inflation starting depth	$[0, +\infty]$	0, 500 m, 1000 m	0
a^h	*e*-folding horizontal scale	$[0, +\infty]$	1000 km	1000 km × cos(ϕ)
a^v	*e*-folding vertical scale	$[0, +\infty]$	10 m as D^o above 220 m 150 m as $D^o = 1000$ m	gridbox thickness
a_b^v	*e*-folding vertical scale for expanding the adjustment at the end of obs	$[0, +\infty]$	1000 m as $D_{\text{bottom}}^o = 2$ km for $a_b^{v,0}$	$4a_b^{v,0} \approx 4$ km for both ENSF and AIEF

b. Tuning of the AIEF

Tuning parameters in this ensemble coupled system for climate time scales requires huge computational cost. To increase the efficiency of parameter tuning, tests are performed with three different time scales. First, 5-day tests with each time step output are compared to choose the candidates of parameter values that produce self-consistent good results, especially not creating any instantaneous upwelling–downwelling. Then 1-month tests with daily outputs are compared across the chosen candidates to ensure the parameter value to be optimal within 1 month. Finally the optimal parameter value is used in a long run (at least 1 yr) to ensure it works for long-term climate estimates.

Generally, a small value for Z_0 means less confidence in σ_t so that even for the upper ocean, the assimilation adjustment is modified by σ_0. For example, if $Z_0 = 0$, the application of Eq. (4) will modify the adjustment of the mixed layer in ensemble filtering by the climatological standard deviation, which may be necessary when a small ensemble size is used. On the contrary, the use of a large Z_0 will keep the temporally evolving character of regression coefficients mostly by filtering. This may be realistic when the ensemble assimilation is performed for a long time and a large ensemble size is used. The a_b^v value reflects the confidence of both the adjustment at the bottom of observed profiles and the ensemble-evaluated correlation in the deep ocean.

Three Z_0 values -0, 500 m, and 1 km, and three a_b^v values $-a_b^{v,0}$, $2a_b^{v,0}$, and $4a_b^{v,0}$ are used in the AIEF tuning. Each value of Z_0 and a_b^v is first tested in a 5-day length. Results show that, generally, for Z_0 (a_b^v), a smaller (larger) value produces better assimilation quality. Then some cross-test experiments combining Z_0 and a_b^v are carried out for 1 month. For example, for the Argo network used in this study in which most of the profiles end at 2 km, 3 values of a_b^v (see Table 1) are applied to case 4 described in section 4a with $D_{\text{bottom}}^o = 2$ km. Finally, five experiments (see Table 1) are compared and discussed in detail. As shown in Fig. 5, when $a_b^v = 4a_b^{v,0}$ ($\approx$4 km at $D_{\text{bottom}}^o = 2$ km), the e-folding depth exceeds the bottom of the model ocean so that the adjustment at the bottom of most Argo profiles is extended to the full ocean depth, while the ramp functions with $a_b^v = a_b^{v,0}$ and $2a_b^{v,0}$ cannot extend the adjustment to the full model depth.

The root-mean-square (rms) errors of oceanic temperature (left) and salinity (right) in different layers produced by these test experiments are shown in Fig. 6, in which the errors of CTL and ENSF are plotted by black dotted and black solid lines as references. From Figs. 6a,b (for top 500 m) and Figs. 6c,d (for 500–1000 m), we find that AIEF consistently strengthens the data

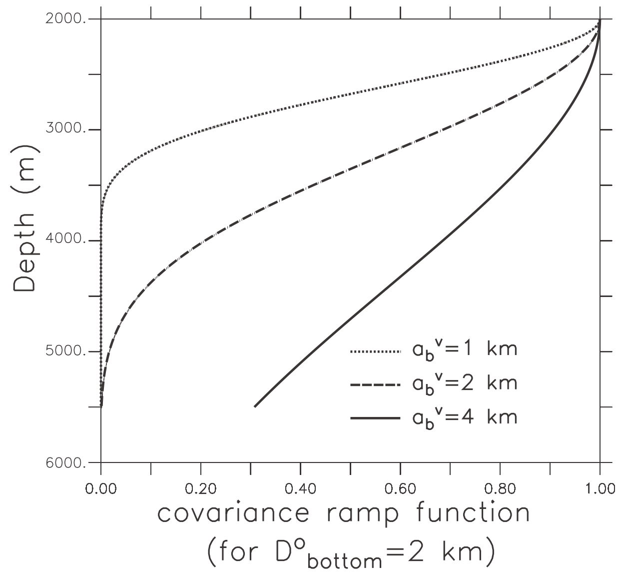

FIG. 5. The covariance ramp function that is used to extend the adjustment at the bottom (usually 2 km) of Argo profiles for a_b^v = 1 km (dotted), a_b^v = 2 km (dashed), and a_b^v = 4 km (solid) [see Eq. (4)].

constraint when Z_0 changes its value from 1 km, 500 m to 0, suggesting that with the small ensemble size, the surface uncertainty is also underestimated to some extent. For the top 500 m, only the rms error of AIEF$_4$, in which the inflation starts at the surface, gets dramatically reduced from ENSF [about 10% (12%) for temperature (salinity)] while in the other 4 experiments—AIEF$_{0,1,2,3}$, which do not inflate until 500 m—errors are reduced by only 4%. Between 500 and 1000 m, for three of the experiments—AIEF$_{2,3,4}$ in which all adjustments below 500 m are inflated—the errors are reduced by 20% and 25% for temperature and salinity, respectively. From Figs. 6a–d, it is observed that the upper ocean also can be corrected slightly because of a substantial correction of the deep ocean, especially for salinity. For example, although the filtering adjustment in the top 500 m in AIEF$_{2,3}$ is the same as in AIEF$_{0,1}$, the rms errors in the top 500 m in AIEF$_{2,3}$ are noticeably smaller than the errors of AIEF$_{0,1}$ because more substantial corrections are made in AIEF$_{2,3}$ than in AIEF$_{0,1}$ below 500 m. Figures 6e–h show that the use of a proper a_b^v value in AIEF is very important to get sufficient corrections for ocean states below 1 km. Both doubling (AIEF$_{1,2}$) and quadrupling (AIEF$_{3,4}$) a_b^v values from $a_b^{v,0}$ produce the same error reduction for the 1–2-km layer [10% (25%) for temperature (salinity)]. However, AIEF$_{3,4}$ nearly double the error reduction for the ocean below 2 km, compared to AIEF$_{1,2}$. This suggests that it is very important to coherently extend the adjustments at the bottom of observed profiles toward deeper depths for estimation of deep-ocean states.

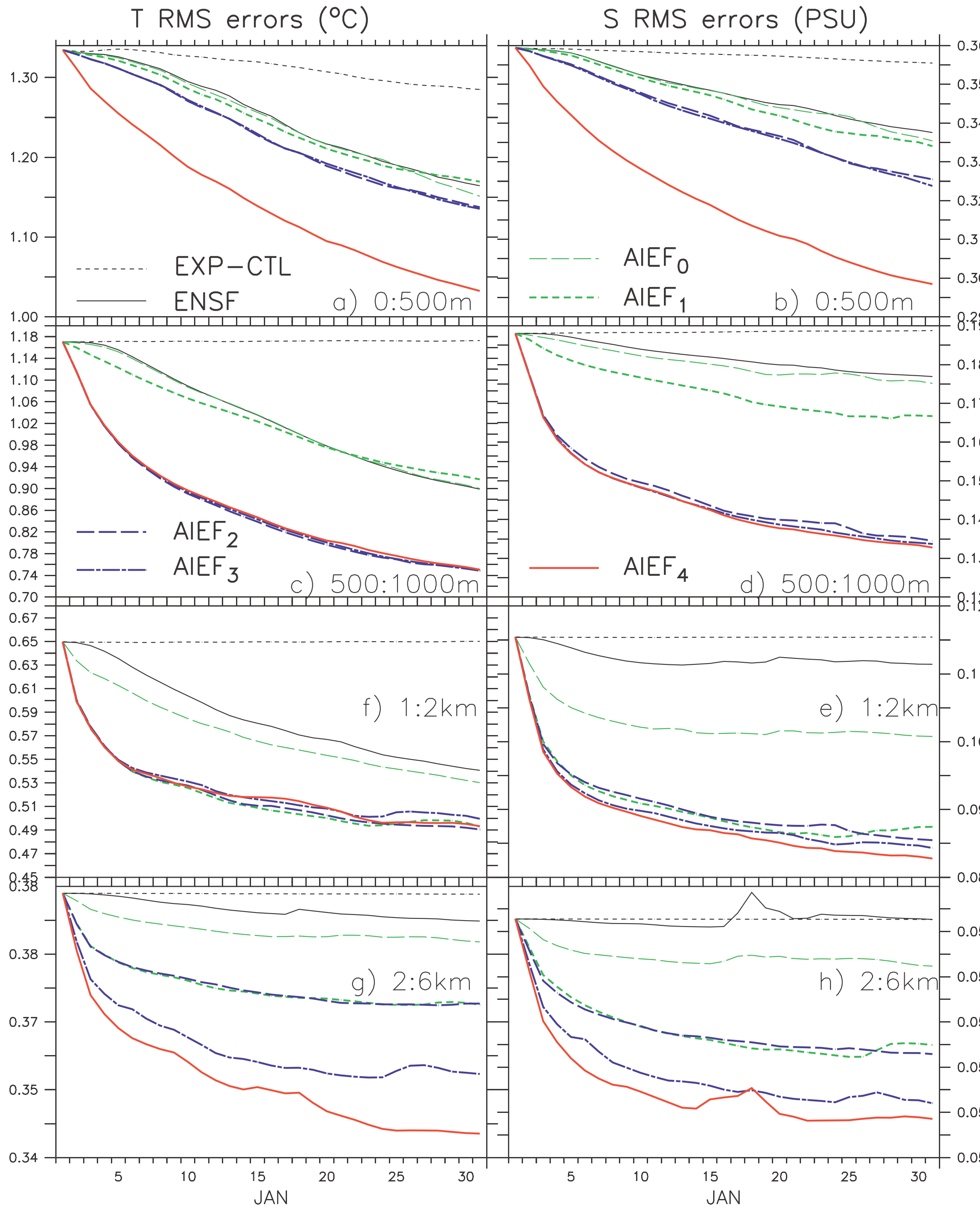

FIG. 6. Time series of global rms errors of (left) temperature and (right) salinity at different layers produced by CTL (black dotted), ENSF (black solid), AIEF with $Z_0 = 1$ km and $a_b^v = a_b^{v,0}$ (AIEF$_0$, green dashed), AIEF with $Z_0 = 1$ km and $a_b^v = 2a_b^{v,0}$ (AIEF$_1$, green dotted), AIEF with $Z_0 = 500$ m and $a_b^v = 2a_b^{v,0}$ (AIEF$_2$, blue dashed), AIEF with $Z_0 = 500$ m and $a_b^v = 4a_b^{v,0}$ (AIEF$_3$, blue dashed–dotted), and AIEF with $Z_0 = 0$ and $a_b^v = 4a_b^{v,0}$ (AIEF$_4$, red solid), within 1-month test experiments: (a),(b) 0–500 m, (c),(d) 500–1000 m, (f),(e) 1–2 km, and (g),(h) 2–6 km.

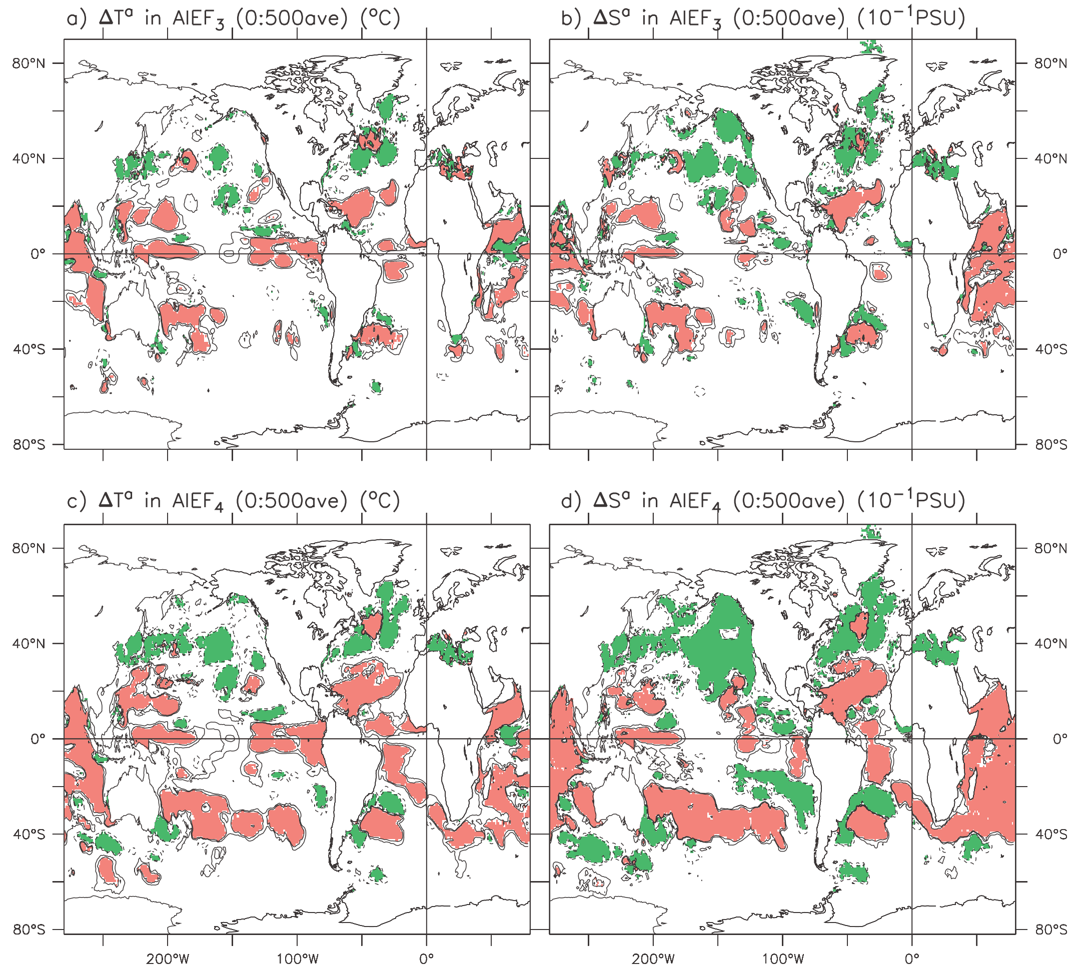

FIG. 7. The horizontal distribution of monthly mean adjustments of (a),(c) temperature and (b),(d) salinity averaged over top 500 m in (a),(b) AIEF$_3$ and (c),(d) AIEF$_4$ in 1-month test experiments. The contour interval is 0.004 (°C 10^{-1} PSU) for (a)–(d). The regions > (<) 0.01 (−0.01) (°C^{-1} 10^{-1} PSU) are shaded as red (green).

Another interesting phenomenon is the interaction of circulations between different layers. None of AIEF$_{0,1,2,3}$ experiments inflates the filtering correction above 500 m. However, it is clear that the errors of top 500 m in AIEF$_{2,3}$ are smaller than the errors in AIEF$_{0,1}$. It is the improved circulation below 500 m in AIEF$_{2,3}$ that results in the improvement of the upper-oceanic circulation. Comparing the errors of AIEF$_3$ and AIEF$_4$, we find that the improvement for the top 500 m in AIEF$_4$ does not have much impact on the layer between 0.5–2 km but improves the layer below 2 km. This can be explained by the effect of JEBAR (see Sarkisyan and Ivanov 1971; Mellor et al. 1982; Myers et al. 1996) in which the top ocean barotropic modes may have a direct influence on the bottom ocean within about the 1-month time scale.

It is also interesting to see how AIEF changes the correction distribution in the filtering. With the same positive and negative correction patterns as in AIEF$_3$, AIEF$_4$ increases the correction magnitude (Fig. 7). In the Pacific and Atlantic Oceans, the major correction-strengthened regions, by order, are the subpolar gyre, subtropical gyre, and the equatorial current system. Correction strengthening is also observed in the Southern Ocean and Indian Oceans. Consistent with the relative rms error reduction for temperature and salinity, the salinity correction is strengthened more than the temperature correction. This suggests that it is more difficult to use the ensemble integration to estimate the variability of the deep-ocean salinity than temperature. Overall, AIEF$_4$ ($Z_0 = 0$ and $a_b^v = 4a_b^{v,0}$) produces the best assimilation quality (Fig. 6). Finally, we examine the rms errors of currents and vertical motions to see if the inflated filtering corrections in five AIEF experiments introduce extra imbalance into oceanic circulations. Generally, all 5 AIEF experiments do not produce any extra imbalance in the circulations above 2 km. In fact, because of the improvement of vertical consistency of filtering corrections (e.g., see the green lines in Figs. 1d,e), currents and vertical motions above 1 km in all AIEF experiments have been improved after about 10 days of spinup. As discussed in section 3b, the accuracy of pressure gradient decreases because of the accumulation of assimilation errors in the vertical integral of water density by depth. Thus, a longer assimilation period is required to reduce the errors of currents and vertical motions in deeper ocean.

Finally, $AIEF_0$ is run for 1 yr (1976), $AIEF_2$ for 3 yr (1977–79), and $AIEF_3$ for 5 yr (1980–84). Two parallel experiments of $AIEF_4$ with the inflation in a global or tropical domain [20°S–20°N, setting 20°N(S)–25°N(S) as a transition region to minimize the shocks] are run for 1985–90 to test the impact of the inflation in extratropics as discussed at the end of section 4a. Results show that the use of $r_{t,0}(T, S)$ in extratropics weakens the signals of strong variability of gyres and produces extra assimilation errors in high latitudes (especially in the North Atlantic Ocean). Therefore $AIEF_4$ with the tropical inflation is run for the final 15 yr until 2000. The results of this long run show AIEF has more potential to improve the salinity assimilation than the temperature (the salinity assimilation is more sensitive to the values of parameters Z_0 and a_b^v; Fig. 8). For example, all $AIEF_{0,1,2,3,4}$ experiments show almost the same level temperature improvement (the maximum error reduction from ENSF is 30%–40% between 2 and 3 km; Fig. 8a) but the inflated filtering with a small a_b^v value cannot improve the salinity estimate deeper than 4 km although it reduces the salinity error up to 40%–50% above 4 km (maximum error reduction appears between 1 and 2 km; Fig. 8b). When a 4-km a_b^v value is used, $AIEF_4$ starts improving the salinity estimate below 4 km, while the currents and vertical motions above 4.5 km are improved dramatically. The maximum error reduction is up to 70% for currents and 50% for vertical motions between 1 and 2 km. Note, as expected, the smallest improvement on velocities is observed at the bottom. We also note that the currents of AIEF are still a little degraded compared to the CTL, reflecting that the data adjustment of AIEF is not completely in the physical balance as in a model simulation.

5. Impact on estimation of climate features and variability

With the knowledge of tuning AIEF described in the last section, the impact of the new algorithm on estimation of climate features and variability is examined by rerunning the 25-yr ENSF and AIEF assimilation experiments with the parameters listed in Table 2. Leaving the first 5 yr as assimilation spinup, all diagnostics and analyses next are based on the assimilation data of last 20 yr (i.e., from 1 January 1981 to 31 December 2000 of the model calendar).

a. *Global annual mean fields*

The subsurface temperature (Figs. 9a,c) and salinity (Figs. 9b,d) errors show that AIEF dramatically reduces the assimilation errors in the tropics. The improvement of the vertical structure of the tropical oceans gives rise to the improvement of oceanic circulations in extratropics. However, perhaps associated with gyres' structures, the improvement is more dramatical for the regions with relatively weak temperature and salinity gradients than the regions with strong temperature and salinity gradients. In particular, over the northwest region of the Atlantic Ocean in the Labrador Sea, the averaged errors over the top 2 km for both temperature and salinity appear a little larger in AIEF than in ENSF. This may be associated with the structure of the Atlantic meridional overturning circulation (AMOC) and its variability, which may require more accurate adjustments as will be discussed in section 5b.

Consistent with the substantial improvement on the vertical structure of the temperature and salinity in the tropical ocean, the errors of the tropical u component and vertical velocities in AIEF are much smaller than in ENSF (Fig. 10). The improvement of currents and vertical motions also gives rise to changes in the thermohaline properties at mid- and high latitudes. These changes are also associated with the changes of other coupled components (e.g., atmospheric conditions) due to the improved SSTs in AIEF (Fig. 9e). The improvement of SSTs in the extratropics is due to more consistent currents and vertical motions in the tropical oceans. The major error reduction of SSTs is observed in the tropical Pacific Ocean, the northern Atlantic Ocean, and the high latitudes of the southern Pacific Ocean. The error reduction of the tropical Pacific reflects the sensitivity of the tropical Pacific SSTs to the undercurrent and upwelling–downwelling. The error reduction in the other two regions reflects the improvement of gyre's structures due to the improved velocities. The improved tropical SSTs must improve precipitation, which leads to the improvement of SSS in the tropical ocean (Fig. 9f). Note that SST and SSS errors over the surface coastal areas of the Atlantic–Antarctic Ocean in AIEF are larger than in ENSF. This is likely associated with sea ice variability in the Antarctic caused by the changes of atmospheric and oceanic conditions in the assimilations. However, further investigations are needed to better explore the associated mechanisms.

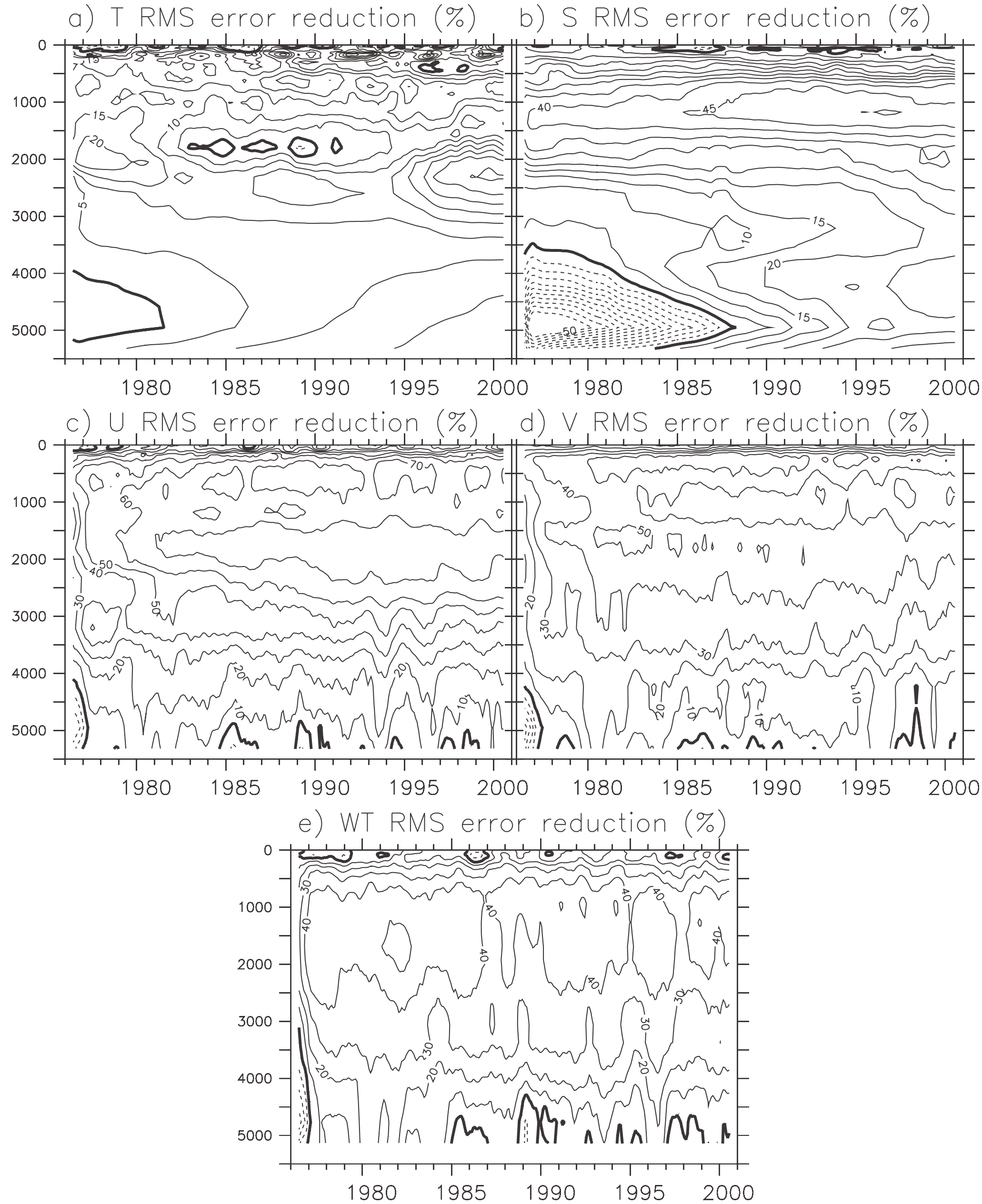

FIG. 8. Time series of the global rms error reduction (%) from ENSF, produced by AIEF for (a) temperature, (b) salinity, (c) u component of currents, (d) v component of currents, and (e) vertical motions. The contour interval is (a),(b) 5% and (c)–(e) 10%. A 10-month running mean is applied for graphing.

Interestingly, as a result of the responses of the atmospheric circulations to improved SSTs, the improvement of meridional wind stress in AIEF is larger than the improvement of zonal wind stress. For example, from ENSF, AIEF reduces the rms error of τ_y by 22% and 11% for the tropical ocean (20°S–20°N) and the World Ocean, respectively, while the corresponding error reduction for τ_x is only 11% and 5%. It is not surprising that the improved currents and vertical motions in AIEF have a stronger impact on τ_y than on τ_x, since τ_x is governed by the meridional gradient of SSTs which represents leading order information in ODA data constraint while τ_y is more tied with the zonal gradient of SSTs, which is associated with more detailed local structures of oceanic circulations. Consistent with the improved SSTs, the regions with great τ_y improvement are, by order, the Indian Ocean, the tropical Pacific Ocean, and the North Atlantic Ocean. The north Indian Ocean is the most

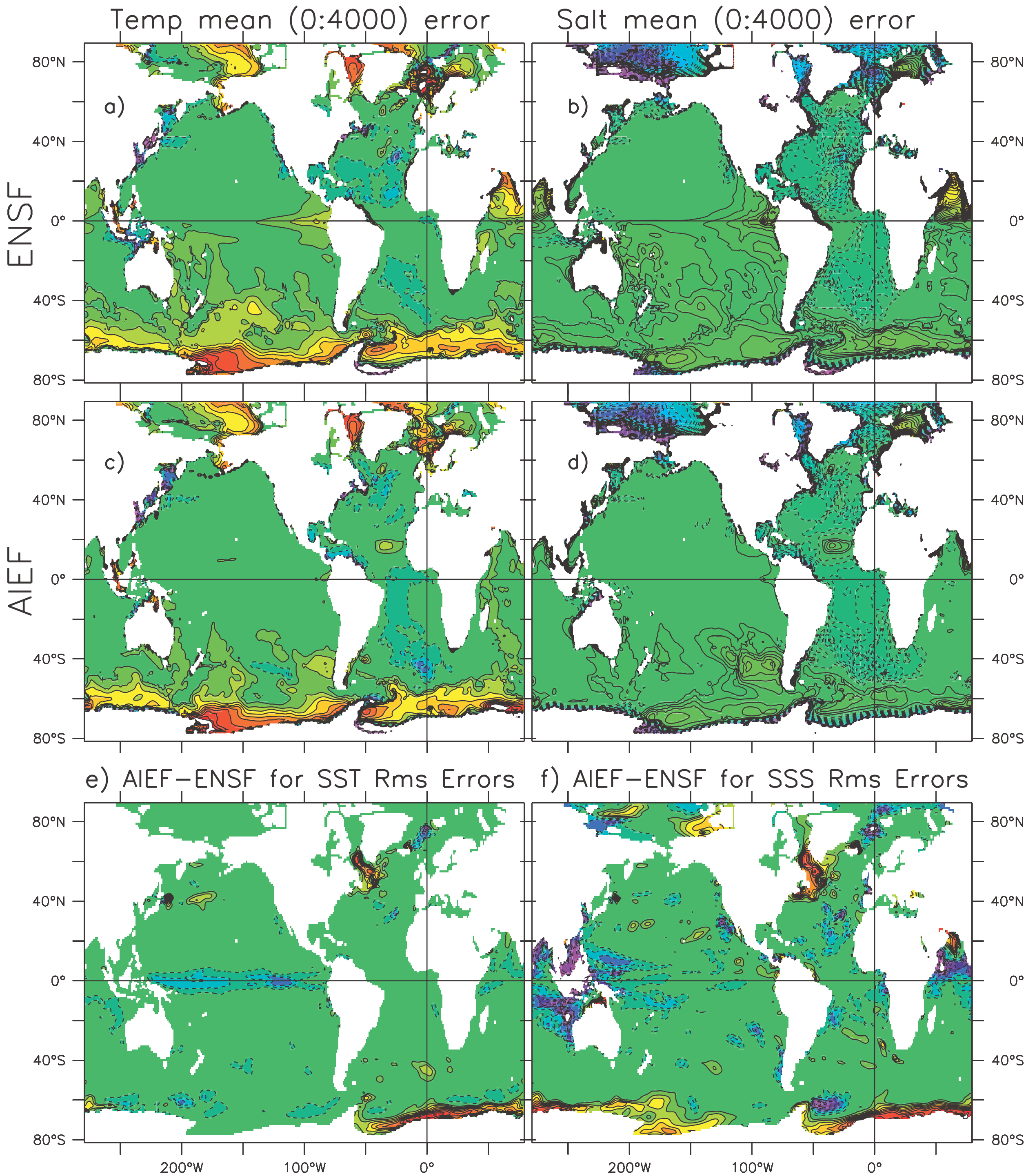

FIG. 9. Time mean errors of the (a),(c) temperature and (b),(d) salinity averaged over 0–4 km in (a),(b) ENSF and (c),(d) AIEF, and the difference of the (e) SST and (f) SSS rms errors between AIEF and ENSF. The contour interval is (a),(b) 0.1°C, (c),(d) 0.01 PSU, (e) 0.2°C, and (f) 0.05 PSU.

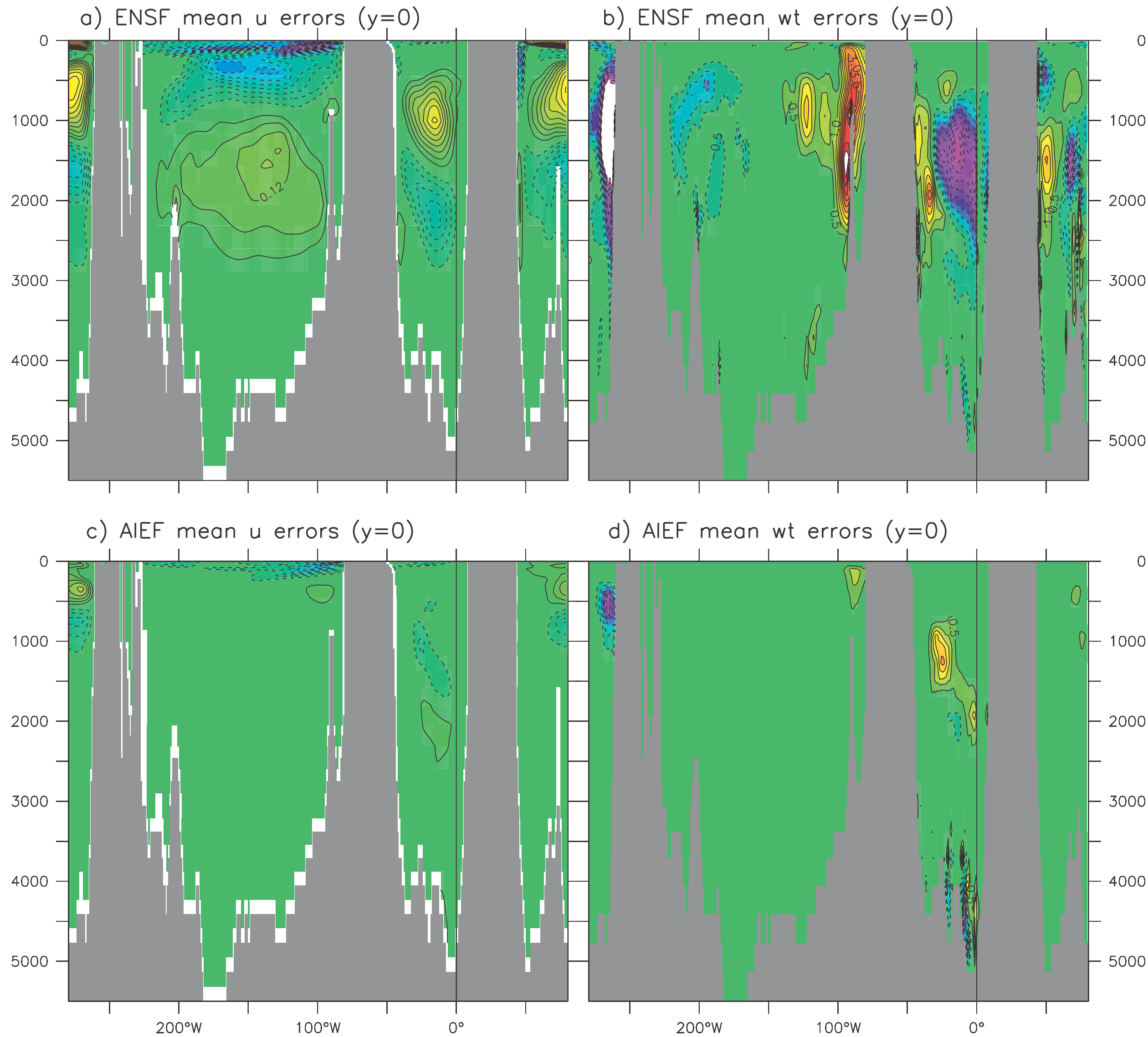

FIG. 10. Time mean (1981–2000) of the assimilation errors of (a),(c) *u*-component and (b),(d) vertical motions on the *x*–*z* plane at the equator produced by (a),(b) ENSF and (c),(d) AIEF. The contour interval is (a),(c) 0.04 m s^{-1} and (b),(d) 0.5 m day^{-1}.

sensitive basin to the covariance formulation used in the assimilation, which will be discussed next.

b. Global/Atlantic overturning and heat–salt transport

The maintenance of data assimilation for general hydrographic features in a coupled system is critically important to initialize numerical climate predictions from seasonal–interannual to multidecadal time scales.

The global overturning in depth space reflects the pole-to-pole circulation associated with the North Atlantic Deep Water. As described in Gnanadesikan et al. (2006), CM2.1 (CTL) and CM2.0 (TRUTH) share a common character, with most of the water downwelling in the northern oceans and traveling all the way to the Southern Ocean. However, CTL shows a stronger and deeper-penetrating overturning at high latitudes. In ENSF, because of too strong spurious upwelling–downwelling in the tropical deep oceans induced by incorrect vertical structures of temperature and salinity, the Pole-to-Pole circulation is broken at the tropical ocean and a reverse circulation appears there. More analyses in the next section will show that it is the north Indian Ocean that makes the tropical reverse circulation, where the coupled balances are very sensitive to the oceanic data constraint, and the vertically inconsistent data adjustment of ENSF creates an imbalance. The improved vertical structure of data constraints in AIEF essentially eliminates the spurious velocity and thus AIEF reduces the global overturning errors greatly. The fact that the AIEF's global overturning error is even a little smaller than the CTL's error, suggests that in a global view, the AIEF adjustments sustain the model balance.

To address the maintenance of AIEF for the balance of oceanic circulations with sea surface wind stresses, we show the global overturning in potential density space (σ_2) (in Figs. 11a,b). In a balanced model simulation, the overturning streamfunction in σ_2 space represents the surface wind-driven circulation, which plays an important role in heat–salt transport (Gnanadesikan et al. 2006; Bocaletti et al. 2005). However, the ENSF-produced spurious velocities in the tropical ocean seriously damage the wind-driven circulation below the mixed layer ($\sigma_2 >$ 1032) and generate a much too strong watermass transformation crossing isopycnal surfaces. This causes a serious error in the northward heat–salt transport at the equatorial region (red lines in Fig. 12b,d) and a reverse circulation (deep water travels from south to north) is generated. Checking the geographic distribution of northward heat–salt transport errors in ENSF, we found that the worst region where the transport is damaged is the north Indian Ocean. Further analyses and diagnostics in section 5d will show that with regard to the vertical consistency of ODA data adjustments, the Indian Ocean is the most sensitive basin, which may be explained by stronger air–sea interactions there. While the spurious velocities are eliminated in AIEF, the watermass transformation represented by the global overturning streamfunction (Fig. 11b) and the direct heat–salt transport (blue lines in Fig. 12b,d) are dramatically improved.

As an important part of global overturning, the AMOC is also interesting to be examined. Because of spurious velocities induced from inconsistent vertical structures of data adjustments in the tropics, ENSF produces a very spurious recirculation in the tropical Atlantic Ocean when it reduces the errors of the AMOC at high latitudes (Fig. 11c). This is consistent with the fact that ENSF produces too strong northward heat and salt transport in the tropical Atlantic Ocean. Because of the improvement of the vertical structure of the tropical Atlantic Ocean, AIEF eliminates the spurious velocities and recirculation (Fig. 11d) and improves the corresponding heat and salt transport accordingly. The time series of the maximum value of the AMOC streamfunction between 40° and 70°N from ENSF (red) and AIEF (blue) (Fig. 11e) show that the improvement of heat and salt transport in low latitudes by AIEF tends to improve the variability of the AMOC, although the AMOC in both assimilations tends to converge toward the truth. Previous studies (Delworth and Greatbatch 2000; Delworth and Dixon 2000) have shown that the surface forcings provided by the atmosphere is important for the interannual variability of the AMOC. In future studies, we shall examine the impact of a fully coupled data assimilation including atmospheric data constraints on the estimate of AMOC variability.

The zonal-depth integrals of the World Ocean heat content (Fig. 12a) and salinity (Fig. 12c) show that although the integral temperature and salinity in the World Ocean converge to TRUTH (black lines) from CTL (green lines) at nearly the same rate in both ENSF (red lines) and AIEF (blue lines), the interior structure of circulations generated by ENSF and AIEF are substantially different. In the future, when evaluating an ODA product, one should be cautious about the convergence of temperature and salinity, since the circulation may not be improved if the convergence lacks vertical coherence. In addition, Fig. 12d shows that in some areas, the errors of the salt transport in AIEF is greater than in ENSF, especially at the midlatitudes of the Southern Hemisphere. We will further investigate the mechanism of this phenomenon in future studies.

c. Pycnocline and sea surface height

Another interesting measure of the assimilation-estimated hydrography is pycnocline depth, which represents a sharp discontinuous boundary layer between light and dense water. The physical property of light (dense) waters above (below) the boundary layer is determined at the surface in low (high) latitudes. Thus, the time mean pycnocline depth at mid- and low latitudes is another interesting synthesis measure of the general transport of heat, salt, and other tracers. Here the pycnocline depth is computed according to the definition of Gnanadesikan (1999) and Park and Bryan (2000) [see also Eq. (B1) in Appendix B].

Given that the water properties at high latitudes are strongly influenced by external forcings—atmospheric fluxes, ice melting, runoff from land, etc.—the estimated pycnocline will only be examined between 40°S and 40°N in this ODA-only study. Compared to CTL, both ENSF and AIEF reduce the error of pycnocline depth to some degree, reducing the rms error by 9% and 45%, respectively. However, ENSF overshoots the correction in most of the basins, with a mean error of −46 m for CTL, 31 m for ENSF, and 10 m for AIEF (see also Fig. 13). The negative errors in most regions in CTL reflect stronger overturning and a deeper penetration in CM2.1 (Gnanadesikan et al. 2006). The overshooting in ENSF is caused by the spurious vertical motions. The lower correlation of the ENSF pycnocline depth with the TRUTH (0.91) than the CTL with the TRUTH (0.96) means that ENSF cannot produce a correct structure of

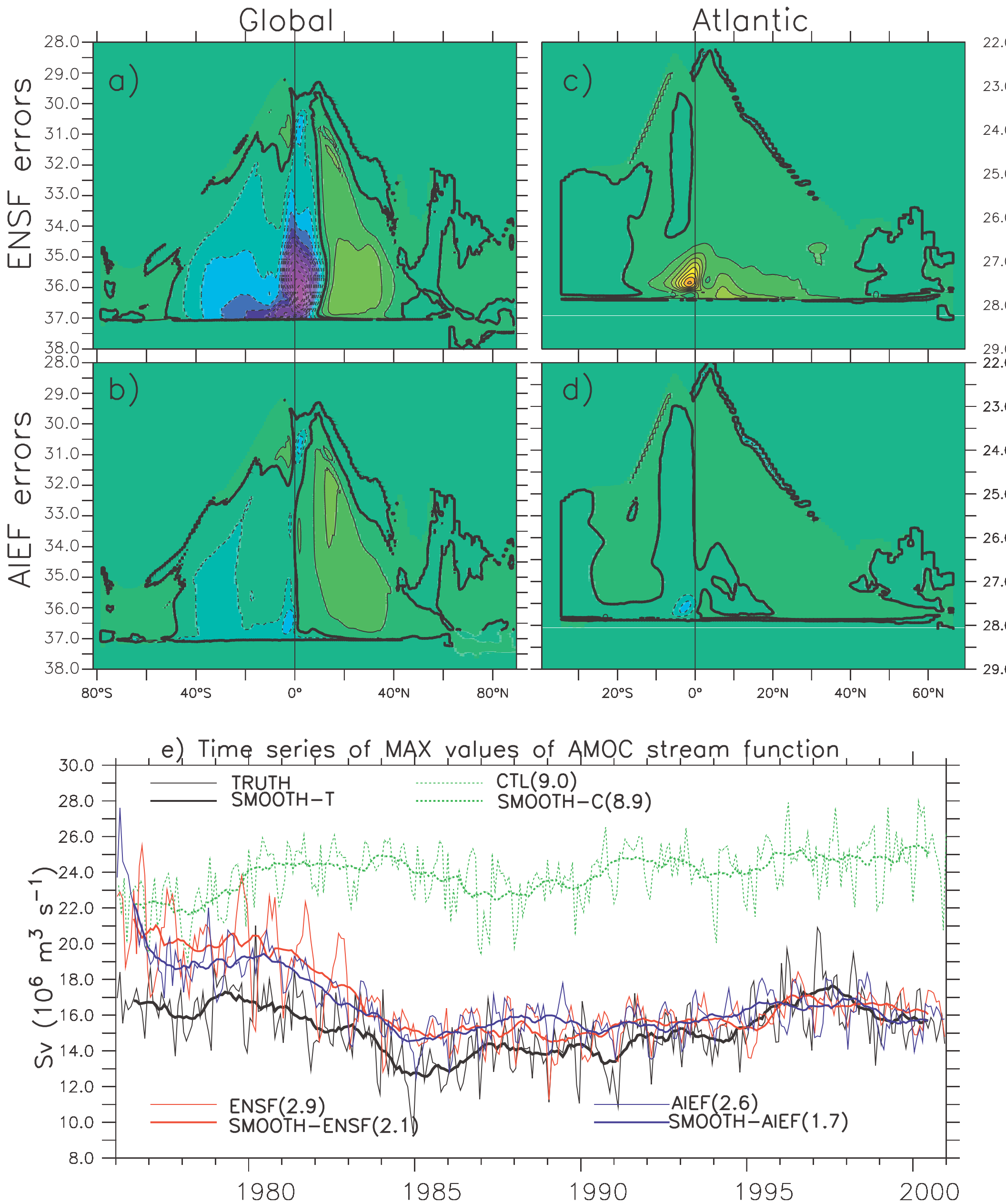

FIG. 11. Time mean of the errors of the (a),(b) global and (c),(d) Atlantic overturning streamfunction in potential density (σ_2) space produced by (a),(c) ENSF and (b),(d) AIEF and (e) time series of the maximum values of the streamfunction of the AMOC (40°–70°N) in AIEF (blue), ENSF (red), TRUTH (black), and CTL (green). The contour interval is 5 (10) Sv as the absolute value is < (>) 30 Sv in (a)–(d). In (e), thick lines represent the 12-month running mean and the number in parentheses is the corresponding rms error.

light–dense waters. With vertically consistent adjustments, AIEF constructs a nearly correct structure of light–dense waters and thus maintains a high correlation between the assimilation pycnocline depth and the TRUTH (0.95).

In a self-balanced oceanic state produced by model simulation, the pycnocline depth is a mirror of the time-mean sea surface height (SSH). Thus, the patterns of SSH differences between the two models can be basically represented by the patterns of the difference of their pycnocline depths. It is expected that the ODA-generated adjustment for oceanic states also maintains this kind of physical balance. Here we define a correlation of time tendencies of pycnocline depth and SSH to estimate the balance sustained by ODA. For example, the correlation computed by 2-decade tendencies (the

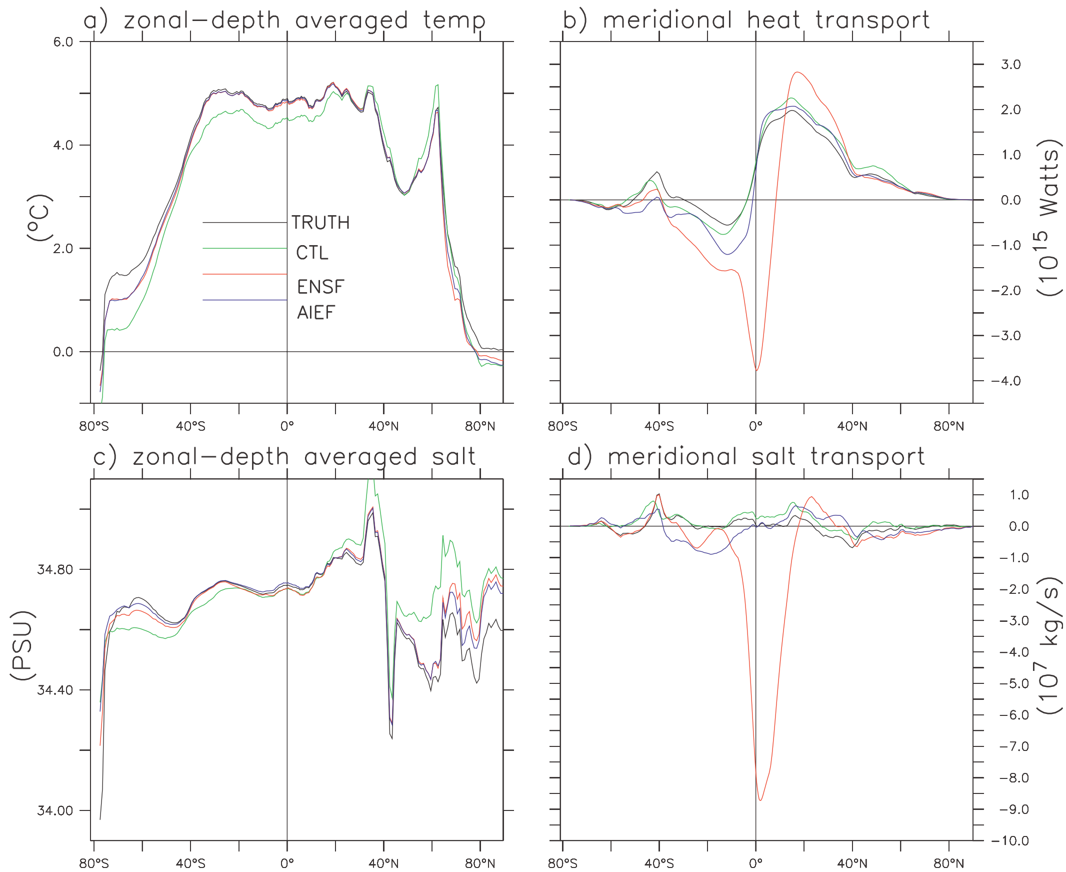

FIG. 12. Variation of the zonal-depth integral of (a) temperature and (b) salinity and northward (c) heat and (d) salt transport with latitudes in CTL (green), ENSF (red), AIEF (blue), and TRUTH (black).

10-yr mean of the 1990s minus the 10-yr mean of the 1980s) of pycnocline depth and SSH is around −0.7 in the two models (−0.73 in CM2.0 and −0.63 in CM2.1). However, the ENSF SSH tendency is persistently contaminated by spurious vertical motions and it completely loses its correlation with the pycnocline depth (−0.07) although ENSF noticeably reduces the errors of SSH from CTL. AIEF enhances the correlation between the tendencies of SSH and pycnocline depth to −0.43 while further reducing the pycnocline and SSH errors.

d. Trends and decadal variability of basin-scale heat content and salinity

From the time series of the temperature and salinity anomalies over the upper 4 km of the ocean in CTL (CM2.1) and TRUTH (CM2.0) (both with respect to the TRUTH's climatology), it is observed that both models show a roughly 0.002°C yr^{-1} warming trend in the World Ocean and they exhibit a roughly −0.32°C (CM2.1–CM2.0) bias with respect to each other (Fig. 14). The Atlantic and Indian Oceans are the major contributors of the warming trend (black lines for TRUTH and green lines for CTL in all panels). The warming trend can be attributed to the common greenhouse gas and natural aerosol external forcings that are used in the simulations of both models. No significant trend is found in the integrated salinity anomaly in individual basins and the World Ocean but a relative bias in salinity (CM2.1 versus CM2.0) is apparent in all basins.

Except for the North Atlantic Ocean, the assimilation model (CM2.1) shows a cold bias compared to TRUTH (CM2.0) in all other basins. The biggest cold bias about −1°C is found in the north Indian Ocean. While we see a nearly uniform cold bias, every basin has its own fresh or saltier bias (Fig. 15). The net result is that the upper-4-km World Ocean maintains a tiny 0.002 PSU fresh bias. Overall, except for a little overshooting in the temperature of the South Atlantic Ocean and the salinity of the North Pacific Ocean, both ENSF (red lines) and AIEF (blue lines) appear to be converging to TRUTH from CTL (i.e., reducing the bias dramatically). For example, the temperature bias of the north Indian Ocean is reduced from −1°C (CTL) to −0.35°C by ENSF, and the salinity bias is reduced from −0.16 to −0.1 PSU by ENSF.

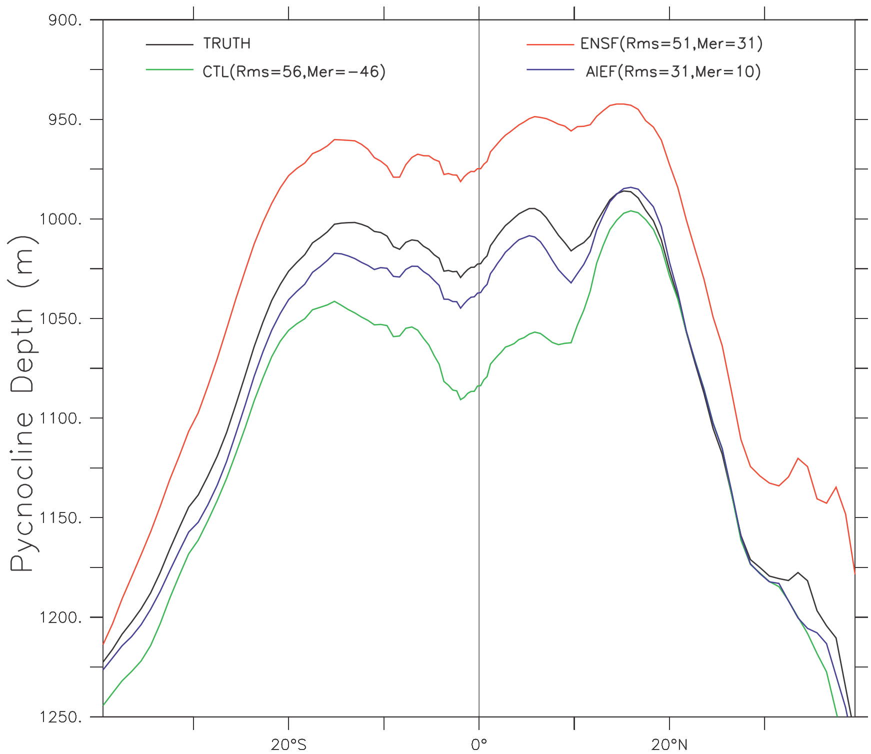

FIG. 13. Variation of the zonal mean pycnocline depth with latitudes in TRUTH (black), CTL (green), ENSF (red), and AIEF (blue). The corresponding root-mean-square (Rms) error and mean error (Mer) are marked in parentheses.

Compared to ENSF, AIEF speeds up the convergence of both temperature and salinity in most of the basins and the World Ocean. Except for the South Atlantic Ocean, AIEF further reduces the temperature bias in every basin and the World Ocean. Because of the averaged effect, no much difference is found for the World Ocean's salinity bias between ENSF and AIEF although the salinity bias in each basin is clearly improved from ENSF to AIEF.

Interestingly, the greatest improvement made by AIEF is found in the north Indian Ocean and the Arctic Ocean for both temperature and salinity. In the north Indian Ocean, the temperature bias is further reduced to −0.05°C from −0.35°C of ENSF while the salinity bias is eliminated almost completely. Another interesting phenomenon in the north Indian Ocean is that the anomalies of both temperature and salinity of ENSF show a computational seasonal cycle–like fluctuation while AIEF does not. Given the fact that the variability of the north Indian Ocean is strongly influenced by the Indian monsoon system, one might attribute this variability to a different seasonal cycle phase of the Indian monsoon driven by the ENSF-generated SSTs. However, neither SSTs nor wind stresses over the north Indian Ocean in ENSF present such a seasonal cycle–like fluctuation. Instead, the SST distributions in ENSF and AIEF are very similar. In fact, this seasonal cycle–like variability in ENSF is induced by the vertically inconsistent data constraint in the ODA algorithm, which persistently conflicts with driving of the monsoon system. These phenomena suggest that the north Indian Ocean is the most sensitive basin to the covariance formulation used in the assimilation. Thus, the atmospheric data constraint in a coupled system is particularly important for oceanic state estimation in this area where air–sea interactions are strong. The advancement of modeling that will substantially reduce model bias over this region will be particularly important for the success of coupled data assimilation. This will be further explored in a future study when the impact of atmospheric data constraint on oceanic climate estimation is examined.

While the ENSF-generated heat content in the other basins converges to TRUTH, the heat content over the Arctic Ocean diverges (the bias is bigger than the CTL and tends to grow), but the AIEF-generated heat content in the Arctic Ocean tends to converge. Since there is no data constraint in the Arctic Ocean, the ENSF divergence or the AIEF convergence has to be the consequence of the model response to the oceanic data constraints in other basins. This is due to either ocean

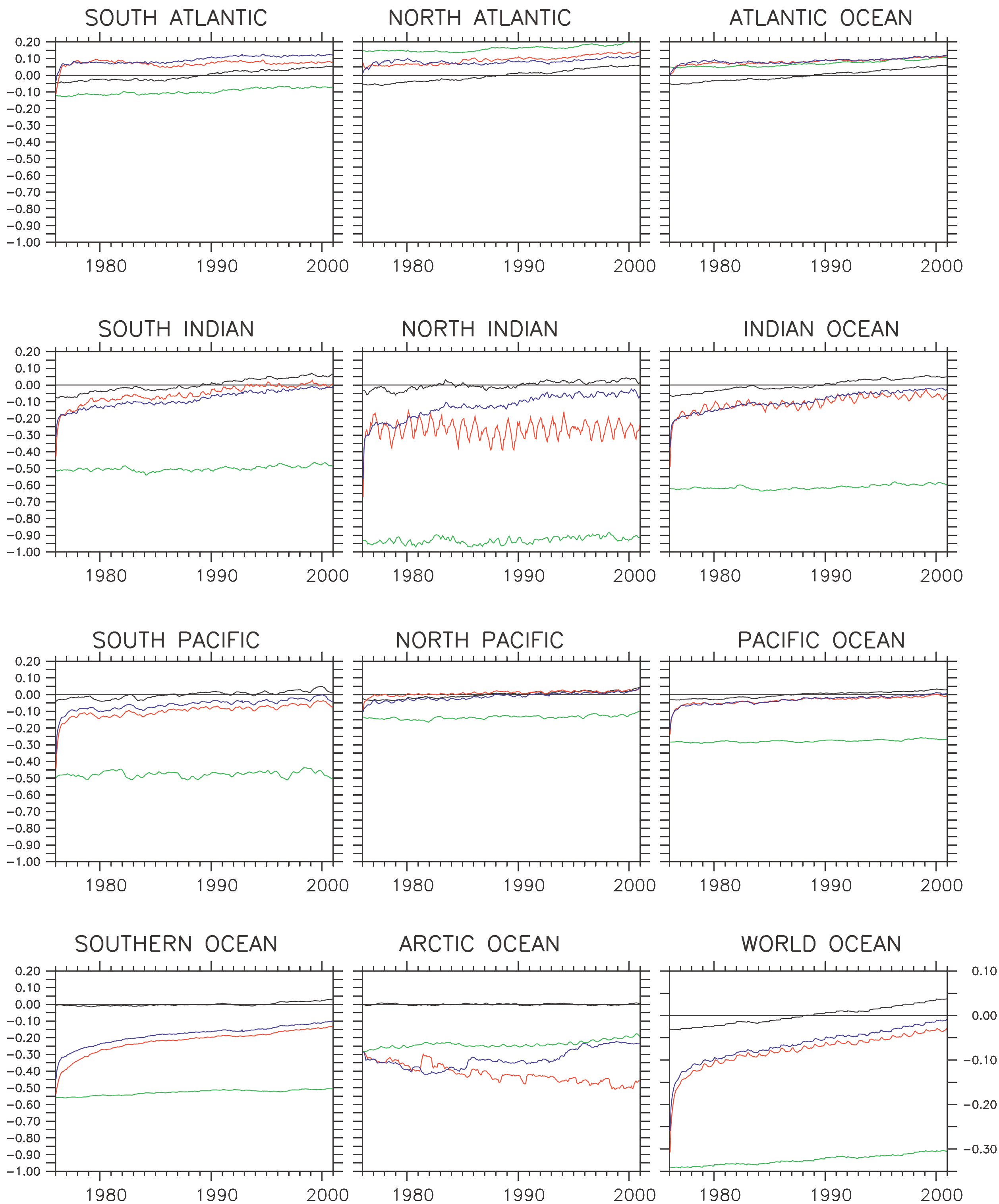

FIG. 14. Time series of the upper-4-km heat content in individual basins and the World Ocean in CTL (green), ENSF (red), AIEF (blue), and TRUTH (black).

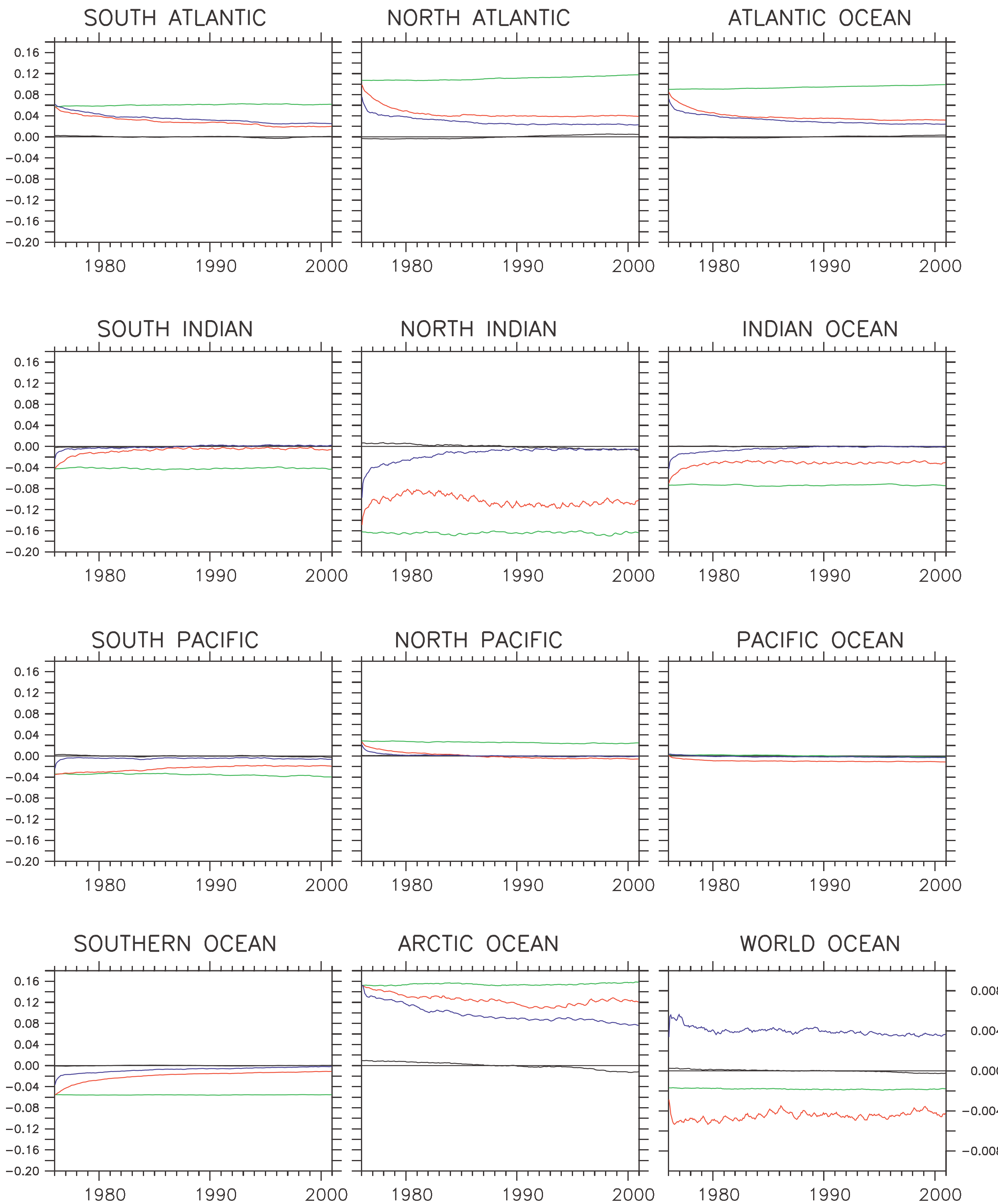

FIG. 15. As in Fig. 14, but for salinity.

interior heat–salt transport or the changes in atmospheric conditions based on different SSTs produced by the corresponding ODA schemes, or both. This aspect will also be further explored in follow-up studies.

e. Variability of El Niño–Southern Oscillation

Figure 10 shows that ENSF and AIEF produce quite different upwelling and undercurrents in tropical oceans.

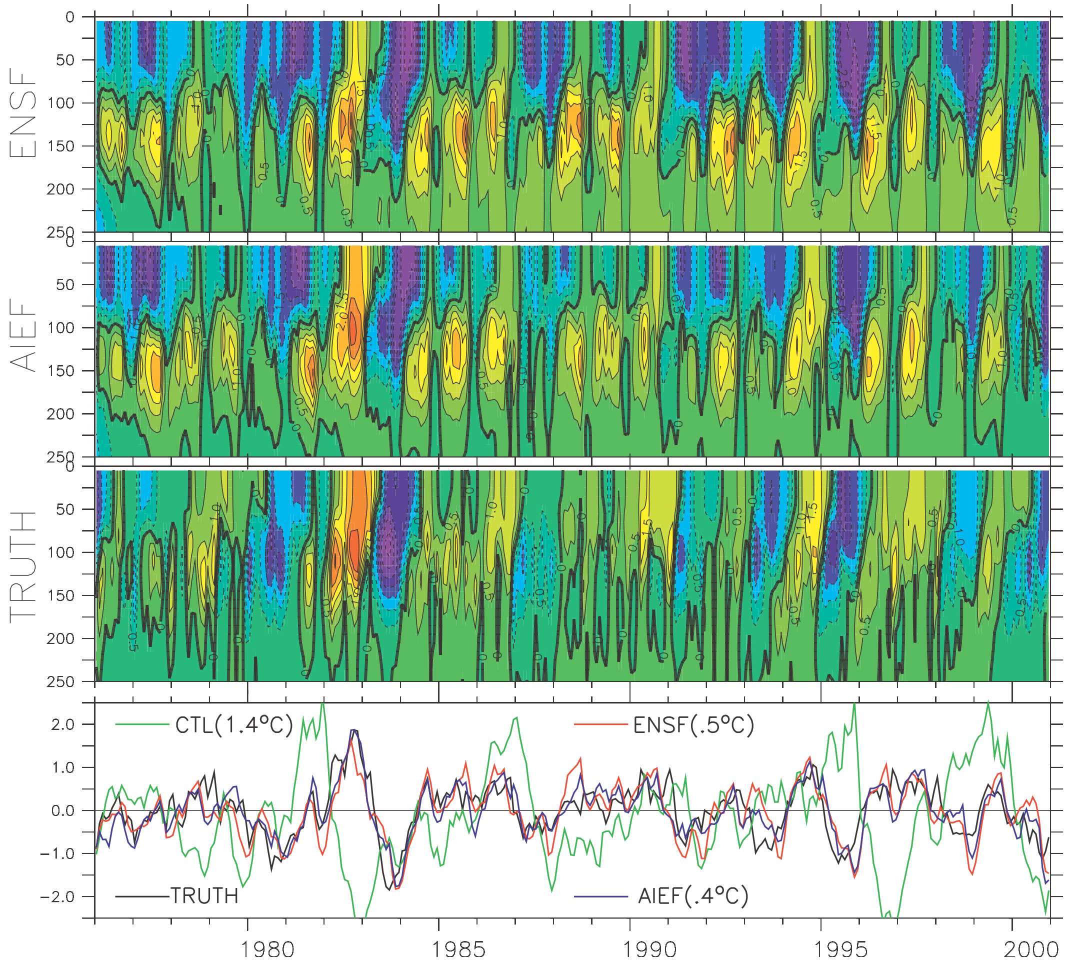

FIG. 16. Time series of the anomalies of the Niño-3.4 temperature in (top to bottom) ENSF, AIEF, TRUTH, and their vertical integrals. The contour interval is 0.5°C in the first three and the number in parentheses in the bottom is the corresponding rms error.

This section discusses the impact of the improved tropical upwelling and undercurrents on the seasonal–interannual variability of the tropical Pacific Ocean.

We focus on the anomalies of the domain-averaged temperature and salinity over Niño-3.4 (5°S–5°N, 170°–120°W; Fig. 16). The two models have totally different ENSO phase and variability (Wittenberg et al. 2006), with ENSO events in CM2.1 (CTL, see the green line in the bottom panel of Fig. 16) being much stronger than in CM2.0 (TRUTH, the red line). Compared to CTL, both ENSF and AIEF reduce the strength and correct the frequency of ENSO events to some degree, decreasing the rms error of anomalies exceeding 50% (64% for temperature and 54% for salinity). While ENSF has larger colder (warmer) errors near surface (thermocline), AIEF further reduces the errors in the phase and strength of ENSO events and produces an extra 20% (12%) error reduction for the temperature (salinity) anomalies from ENSF.

6. Summary and discussion

An ensemble filter uses ensemble model integrations to instantaneously evaluate background error covariances for assimilating observations into the model ensemble. The temporally evolving error statistics are good for capturing upper-ocean variability in ocean data assimilation. The statistical character of oceanic circulations varies from location to location, especially at depth. For example, the variance of the tropical ocean temperature, salinity, and currents is mostly concentrated above 500 m, and the ensemble spread decreases dramatically below the thermocline. The subtropical and subpolar gyres can extend the spread much deeper in the extratropics. Generally, deep-ocean circulations are dominated by lower-frequency fluctuations, making it difficult for an ensemble filter to capture the signals of interest smoothly because of the difficulties to estimate the long time-scale variability, especially in the presence of model biases. The infrequent observations in the deep ocean combined with model bias also complex the problem.

Different from previous work within a perfect model study framework using a single model (CM2.0) (Zhang et al. 2007, 2009), to examine the impacts of model biases on ocean data assimilation with the ensemble filter, this study designed a biased-twin experiment framework using two CGCMs (CM2.0 and CM2.1). One of them—the CM2.0—is used to produce the ''truth'' and ''observations,'' and the other—the CM2.1—is used to assimilate the simulated observations that sample the truth according to an observing network (the 2005 Argo in this case). The results show that a traditional ensemble filter (ENSF) can lead to vertical inconsistency in the analysis solution with a biased assimilation model using a limited ensemble size and within a relatively short ensemble assimilation time, as the upper ocean is assimilated more effectively than the deep ocean. The vertical inconsistency between the well-constrained upper ocean and the poorly constrained deep ocean generates spurious currents and vertical velocities. An adaptively-inflated ensemble filter (AIEF) has been designed to improve the vertical consistency of the filtering ocean data assimilation. A ''climatological'' standard deviation that is adaptively updated by observational information is used to inflate the prior ensemble in the filtering. While maintaining the physical balance required by model dynamics through the interensemble structure of the assimilation model, the new algorithm coherently increases data constraints in the deep ocean according to the climatological variance of local ocean circulations as well as appropriate vertical localization scales. Thus, the new algorithm enhances the consistency of adjustments to the whole water column.

Experimental results show that compared to the ENSF, the AIEF improves the assimilation quality dramatically. It reduces the rms errors of deep ocean (1–4 km) by 30%–40% for temperature and 40%–50% for salinity. The AIEF-generated density distribution improves the estimates of currents and vertical motions greatly. Relative to the ENSF, the AIEF reduces the rms errors of horizontal currents up to 70% and the rms errors of vertical velocities up to 50%. Furthermore, the AIEF dramatically improves the tropical undercurrent, upwelling, and associated Western Boundary Current systems as well as the subtropical gyre structure. Consequently, the hydrographic features of the World Ocean such as global overturning, pycnocline depth, and meridional heat–salt transport are better constructed. Consistently, the estimate of the climatological feature and variability of the Atlantic meridional overturning circulation (AMOC) is also improved. Coherently, the estimates of longtime trends of basin-scale heat content and salinity as well as seasonal–interannual variability of the tropical ocean are much improved. Results also show that the Indian Ocean, especially the north Indian Ocean where stronger atmospheric feedbacks are involved, is the most sensitive basin to the covariance formulation used in the assimilation.

This study only focuses on the results of ODA using a coupled system under a biased-twin experiment framework, in which the AIEF only implements the inflation in the tropical band and leaves the filtering in mid- to high-latitude areas uninflated. On the one hand, the biased-twin experiment could serve as a test bed to locate problems and evaluate potential solutions for the real assimilation experiment using instrumental data. For example, how to extend the inflation to the extratropical areas for further improving the assimilation quality is worth to be explored within the biased-twin experiment framework. In addition, the coupled data assimilation in the biased-twin experiment that includes the atmospheric data constraint shows that the reverse circulation at tropics in the global overturning produced by ENSF is weak. However, the recirculation in the AMOC in the tropical Atlantic Ocean is still strong. This suggests that while the atmospheric data constraint in a fully coupled data assimilation experiment may relax the destruction of coupled balances in the north Indian Ocean to some degree, an inconsistency between upper- and deep-ocean data constraints still exists in the case with a strong surface forcing correction. On the other hand, with these knowledge learned from the biased-twin experiments, the coupled reanalysis using the instrumental oceanic data and the National Centers for Environmental Prediction–National Center for Atmospheric Research (NCEP–NCAR) atmospheric reanalysis (Kalnay et al. 1996) has shown significantly improved estimation for oceanic states. The improvements are not only for the equatorial undercurrent and upwelling but also for global climate features such as the global overturning and heat–salt transport as well as the Atlantic meridional overturning. These results may hold some promise for longer-term climate projections, for example, the prediction of decadal and multidecadal fluctuations in the AMOC. Trial prediction experiments trying to simulate AMOC decadal variability show that the performance of AIEF is superior to that of ENSF but a substantial model drift after initialization still exists. Perhaps an assimilation scheme with adaptive bias corrections (Dee and Silva 1998; Bell et al. 2004; Dee 2005; Kepenne et al. 2005; Balmaseda et al. 2007; Danforth and Kalnay 2008) implemented in both atmosphere and ocean data assimilations (e.g., Chen et al. 2000) and pursuing better balanced oceanic analyses (e.g., Gerrit et al. 2002) would be necessary to create further improvement. Furthermore, a new data assimilation approach with adaptive parameter correction (Zhang et al. 2010, manuscript submitted to *Mon. Wea. Rev.*) that adaptively performs both state and parameter estimations using observed data is expected to further relax the model drift during prediction.

It is worth mentioning that the results of this study are based on a relatively small ensemble size compared to the degrees of the coupled system. In the future when the computational resource is progressively advanced, the impact of ensemble sizes on the AIEF shall be fully explored. Also, in the future when the computational resource is allowed, other approaches that deal with deep-ocean biases such as using a larger and low mode initial condition for the errors at depth (e.g., Lermusiaux 2002) and/or a stochastic error model at depths (e.g., Lermusiaux 2006) are worth being implemented for improving the coupled data assimilation system.

Acknowledgments. Special thanks go to Drs. Rym Msadek, Bill Stern, Andrew Wittenberg, and Matthew J. Harrison for their thorough examination on the earlier version, which is very helpful to improve the manuscript. The authors also thank Drs. Qian Song and Tony Gorden for their comments on the earlier version. Thanks go to Drs. Guijun Han and You-Soon Chang for their suggestions in processing observation data during their visiting at GFDL. The authors thank two anonymous reviewers for their thorough examination and comments that were very useful for improving the manuscript.

APPENDIX A

Function $\Omega(a, d)$

$$\Omega(a,d)=\begin{cases}-\frac{1}{4}\left(\frac{d}{a}\right)^5+\frac{1}{2}\left(\frac{d}{a}\right)^4+\frac{5}{8}\left(\frac{d}{a}\right)^3-\frac{5}{3}\left(\frac{d}{a}\right)^2+1, & 0\le d\le a;\\ \frac{1}{12}\left(\frac{d}{a}\right)^5-\frac{1}{2}\left(\frac{d}{a}\right)^4+\frac{5}{8}\left(\frac{d}{a}\right)^3+\frac{5}{3}\left(\frac{d}{a}\right)^2-5\left(\frac{d}{a}\right)+4-\frac{2}{3}\left(\frac{d}{a}\right)^{-1}, & a<d\le 2a;\\ 0, & d>2a.\end{cases} \tag{A1}$$

Here d is either a Euclidean spatial distance (horizontal or vertical), or a time difference, between the model grid point and the observation location; and a controls the observational impact window.

APPENDIX B

Pycnocline Depth

Following Gnanadesikan (1999) and Park and Bryan (2000), the pycnocline depth Z_σ is defined here as

$$Z_\sigma=\int_{z=-H}^{0}\Delta\sigma_2 z\,dz\bigg/\int_{z=-H}^{0}\Delta\sigma_2\,dz, \tag{B1}$$

where σ_2 is potential density referenced to 2 km and $\Delta\sigma_2=\sigma_2(z)-\sigma_2(z_{\max})$ ($z_{\max}=2.5$ km).

REFERENCES

Anderson, J. L., 2001: An ensemble adjustment Kalman filter for data assimilation. *Mon. Wea. Rev.,* **129,** 2884–2903.

——, 2003: A local least squares framework for ensemble filtering. *Mon. Wea. Rev.,* **131,** 634–642.

——, 2007: An adaptive covariance inflation error correction algorithm for ensemble filters. *Tellus,* **59A,** 210–224.

——, and S. L. Anderson, 1999: A Monte Carlo implementation of the nonlinear filtering problem to produce ensemble assimilations and forecasts. *Mon. Wea. Rev.,* **127,** 2741–2758.

——, T. Hoar, K. Raeder, N. Collins, R. Torn, and A. F. Arellano, 2009: The data assimilation research testbed: A community data assimilation facility. *Bull. Amer. Meteor. Soc.,* **90,** 1283–1296.

Balmaseda, M. A., D. Dee, A. Vidard, and D. T. Anderson, 2007: A multivariate treatment of bias for sequential data assimilation: Application to the tropical oceans. *Quart. J. Roy. Meteor. Soc.,* **133,** 167–179.

Bell, M. J., M. J. Martin, and N. K. Nichols, 2004: Assimilation of data into an ocean model with systematic errors near the equator. *Quart. J. Roy. Meteor. Soc.,* **130,** 873–893.

Bocaletti, G., R. Ferrari, A. Adcroft, D. Ferreira, and J. Marshall, 2005: The vertical structure of ocean heat transport. *Geophys. Res. Lett.,* **32,** L10603, doi:10.1029/2005GL022474.

Chen, D., M. A. Cane, S. E. Zebiak, R. Canizares, and A. Kaplan, 2000: Bias correction of an ocean-atmosphere coupled model. *Geophys. Res. Lett.,* **27** (16), 2585–2588.

Cherupin, D., J. A. Carton, and D. Dee, 2005: Forecast model bias correction in ocean data assimilation. *Mon. Wea. Rev.,* **133,** 1328–1342.

Counillon, F., P. Sakov, and L. Bertino, 2009: Application of a hybrid EnKF-OI to ocean forecasting. *Ocean Sci.,* **5,** 389–401.

Danforth, C. M., and E. Kalnay, 2008: Impact of online empirical model correction on nonlinear error growth. *Geophys. Res. Lett.,* **35,** L24805, doi:10.1029/2008GL036239.

Dee, D. P., 2005: Bias and data assimilation. *Quart. J. Roy. Meteor. Soc.,* **131,** 3323–3343.

——, and A. M. D. Silva, 1998: Data assimilation in the presence of forecast bias. *Quart. J. Roy. Meteor. Soc.,* **124,** 269–295.

Delworth, T. L., and K. Dixon, 2000: Implications of the recent trend in the Arctic–North Atlantic oscillation for the North Atlantic thermohaline circulation. *J. Climate,* **13,** 3721–3727.

——, and R. J. Greatbatch, 2000: Multidecadal thermohaline circulation variability driven by atmospheric surface flux forcing. *J. Climate,* **13,** 1481–1495.

——, and Coauthors, 2006: GFDL CM2 global coupled climate models. Part I: Formulation and simulation characteristics. *J. Climate,* **19,** 643–674.

Gerrit, B., M. A. Balmaseda, F. Vossepoel, G. J. Van Oldenborgh, and P. J. Van Leeuwen, 2002: Balanced ocean-data assimilation near the equator. *J. Phys. Oceanogr.,* **32,** 2509–2519.

GFDL Global Atmospheric Model Development Team, 2004: The new GFDL global atmosphere and land model AM2/LM2: Evaluation with prescribed SST simulations. *J. Climate,* **17,** 4641–4673.

Gnanadesikan, A., 1999: A simple predictive model for the structure of the oceanic pycnocline. *Science,* **283,** 2077–2079.

——, and Coauthors, 2006: GFDL CM2 global coupled climate models. Part II: The baseline ocean simulation. *J. Climate,* **19,** 675–697.

Griffies, S. M., 2005: Some ocean model fundamentals. *Ocean Weather Forecasting: An Integrated View of Oceanography,* E. P. Chassignet and J. Verron, Eds., Springer, 19–74.

Hunke, E. C., and J. K. Dukowicz, 1997: An elastic-viscous-plastic model for sea ice dynamics. *J. Phys. Oceanogr.,* **27,** 1849–1867.

Jazwinski, A. H., 1970: *Stochastic Processes and Filtering Theory*. Academic Press, 376 pp.

Kalnay, E., 2003: *Atmospheric Modeling, Data Assimilation and Predictability*. Cambridge University Press, 341 pp.

——, and Coauthors, 1996: The NCEP/NCAR 40-Year Reanalysis Project. *Bull. Amer. Meteor. Soc.,* **77,** 437–471.

Kepenne, C. L., M. M. Rienecker, N. P. Kurkowski, and D. A. Adamec, 2005: Ensemble Kalman filter assimilation of temperature and altimeter data with bias correction and application to seasonal prediction. *Nonlinear Processes Geophys.,* **12,** 491–503.

Leslie, W. G., A. R. Robinson, P. J. Haley, O. Logoutov, P. Moreno, P. E. J. Lermusiaux, and E. Coehlo, 2008: Verification and training of real-time forecasting of multi-scale ocean dynamics for MREA. *J. Mar. Syst.,* **69,** 3–16.

Lermusiaux, P. F. J., 2002: On the mapping of multivariate geophysical fields: sensitive to size, scales and dynamics. *J. Atmos. Oceanic Technol.,* **19,** 1602–1637.

——, 2006: Uncertainty estimation and prediction for interdisciplinary ocean dynamics. *J. Comput. Phys.,* **217,** 176–199.

——, 2007: Adaptive modeling, adaptive data assimilation and adaptive sampling. *Physica D,* **230,** 172–196.

Lin, S.-J., 2004: A ''vertically Lagrangian'' finite-volume dynamical core for global models. *Mon. Wea. Rev.,* **132,** 2293–2307.

Mellor, G., C. R. Mechoso, and E. Keto, 1982: A diagnostic calculation of the general circulation of the Atlantic Ocean. *Deep-Sea Res.,* **29,** 1171–1192.

Myers, P. G., A. F. Fanning, and A. J. Weaver, 1996: JEBAR, bottom pressure torque, and Gulf Stream separation. *J. Phys. Oceanogr.,* **26,** 671–683.

Park, Y.-G., and K. Bryan, 2000: Comparison of thermally driven circulations from a depth-coordinate model and an isopycnal-layer model. Part I: Scaling-law sensitivity to vertical diffusivity. *J. Phys. Oceanogr.,* **30,** 590–605.

Randall, D. A., and Coauthors, 2007: Climate models and their evaluation. *Climate Change 2007: The Physical Science Basis,* S. Solomon et al., Eds., Cambridge University Press, 589–662.

Sarkisyan, A. S., and V. F. Ivanov, 1971: Joint effect of baroclinicity and bottom relief as an important factor in the dynamics of sea currents. *Izv. Atmos. Ocean Phys.,* **7** (2), 172–188.

Stouffer, R. J., A. Weaver, and M. Eby, 2004: A method for obtaining pretwentieth century initial conditions for use in climate change studies. *Climate Dyn.,* **23,** 327–339.

Uzunoglu, B., S. J. Fletcher, M. Zupanski, and I. M. Navon, 2007: Adaptive ensemble reduction and inflation. *Quart. J. Roy. Meteor. Soc.,* **133,** 1281–1294.

Winton, M., 2000: A reformulated three-layer sea ice model. *J. Atmos. Oceanic Technol.,* **17,** 525–531.

Wittenberg, A. T., A. Rosati, N.-G. Lau, and J. J. Ploshay, 2006: GFDL's CM2 global coupled climate models. Part III: Tropical Pacific climate and ENSO. *J. Climate,* **19,** 675–697.

Wyman, B. L., 1996: A step-mountain coordinate general circulation model: Description and validation of medium-range forecasts. *Mon. Wea. Rev.,* **124,** 102–121.

Zhang, S., and J. L. Anderson, 2003: Impact of spatially and temporally varying estimates of error covariance on assimilation in a simple atmospheric model. *Tellus,* **55A,** 126–147.

——, M. J. Harrison, A. T. Wittenberg, and A. Rosati, 2005: Initialization of an ENSO forecast system using a parallelized ensemble filter. *Mon. Wea. Rev.,* **133,** 3176–3201.

——, ——, A. Rosati, and A. T. Wittenberg, 2007: System design and evaluation of coupled ensemble data assimilation for global oceanic climate studies. *Mon. Wea. Rev.,* **135,** 3541–3564.

——, A. Rosati, M. Harrison, R. Gudgel, and W. Stern, 2008: GFDL's coupled ensemble data assimilation system, 1980–2006: Coupled reanalysis and its impact on ENSO forecasts. Preprints, *Third WCRP Int. Conf. on Reanalysis,* Tokyo, Japan, WCRP, 1–3.

——, ——, and M. J. Harrison, 2009: Detection of multi-decadal oceanic variability by ocean data assimilation in the context of a ''perfect'' coupled model. *J. Geophys. Res.,* **114,** C12018, doi:10.1029/2008JC005261.